

Role of strain-rate partitioning in aseismic strain localization: implications for the Karakoram Shear Zone, India

Subham Bose, Vikas Adlakha^{*}, Shailendra Pundir

Wadia Institute of Himalayan Geology, Dehradun, India

Correspondence to: vikas.himg@gmail.com

Abstract

Shear zones in the earth's crust commonly deform by aseismic creep processes which involve localization of strain at varying rates across the shears. Therefore, it is of key importance to quantify the order of strain-rate variation to understand whether deformation was accommodated solely by aseismic or by simultaneous seismic and aseismic slip. The present study demonstrates partitioning of strain-rate between coarse-grained quartz rich layers (CGQL) and amphibole-biotite rich layers (AMBIORL) due to mineralogical and consequently rheological heterogeneities within the mylonitized amphibolites of the Karakoram Shear Zone (KSZ), India. Variations in modal proportion of quartz across the layers resulted in a lower strain rate per unit area accommodated by quartz, in the CGQL than in the AMBIORL that deformed a rate, 2.34-3.43 times higher than the CGQL. Therefore, a considerably higher proportion of dynamically recrystallized quartz nucleated in the AMBIORL. Combined analyses of the proportion of strain-rate partitioning with previously calculated bulk strain-rates suggest that both the CGQL and the AMBIORL deformed by aseismic creep. Thus, strain-rate partitioning due to mineralogical or lithological heterogeneity is a feasible mechanism for strain localization during aseismic creep. Calculated proportion of strain-rate partitioning, when extrapolated to two adjacent lithologically distinct hypothetical layers (at a regional scale), yields differences of 100-200

kilometres, in displacement accommodated by the two layers. Thus, this study suggests that variation in offsets of streams and marker beds, along widely separated segments of the KSZ might well be the manifestations of strain-rate partitioning in the middle-lower crust.

Plain Language Summary

Variation in strain-rate at the microscopic scale, or strain-rate partitioning across two adjacent mineralogically distinct layers, occurred in the mylonitized amphibolites of the KSZ, due to differences in rheological responses of the layers and the modal proportion of quartz. Strain-rate partitioning resulted in a bimodal grain-size distribution of quartz. Calculated proportion of partitioning of strain-rate between the two mineralogically distinct adjacent layers suggest that both underwent extremely slow slip deformation by aseismic creep. Thus, strain-rate partitioning is a feasible mechanism of strain localization across mineralogically and lithologically distinct zones at diverse scales (micro- to regional) during aseismic creep and can be an important attribute for the considerably variable displacements and hence, offsets along widely separated segments of shears, like the KSZ.

1. Introduction

Strain-rate has always been a parameter of interest in both natural as well as experimental deformation studies, for example, Boutonnet et al. (2013); Fagereng & Biggs (2019); Gleason & Tullis (1995); Hirth et al. (2001); Peternell et al. (2019); Pfiffner & Ramsay (1982); Takahashi et al. (1998). Estimation of strain-rates can be especially significant while investigating active tectonic zones from the combined perspective of the nature and extent of strain accumulation and release (Cannon et al., 2018; Fan and Murphy, 2021; Ojo et al., 2021; Tamura et al., 2020). While strain-rates on the surface are estimated using geodetic techniques (e.g., Gauhlat et al., 2013; Kreemer et al., 2014; Panda et al., 2020) rates of middle to lower crustal deformations are calculated mainly based on deformed quartz, for example strain-rate

48 formulations of Takahashi (1998) as well as the recent Quartz-strain-rate-metry (QSR)
49 technique devised by Boutonnet et al. (2013). Idea about strain rates becomes increasingly
50 essential when the deformation temperatures are estimated based on the observed
51 microstructures of minerals like feldspar (Ji, 1998; Pryer, 1993; Rosenberg & Stunitz, 2003)
52 and quartz (Hirth & Tullis, 1992; Stipp et al., 2002; Stipp et al., 2010). Although with
53 increasing temperature and decreasing strain rates there is a transition in the recrystallization
54 mechanism of quartz from bulging (BLG) through sub-grain rotation (SGR) to Grain Boundary
55 Migration (GBM) (Law, 2014; Stipp et al., 2002; 2010), not always this transition occurs at
56 conventional strain-rates of Pfiffner & Ramsay, 1982. This is particularly emphasized by Law
57 (2014) by extrapolating the regimes of operation of BLG, SGR and GBM for quartz to the
58 conditions of prevalence of experimental strain-rates. Apart from quantitative estimation of
59 strain-rates (Boutonnet et al., 2013; Pfiffner & Ramsay, 1982; Takahashi et al., 1998) it is also
60 important to characterize high and low strain-rate regimes across natural shear zones. In this
61 context, variation in strain-rates within regional scale ductile shear zones has been documented
62 qualitatively, by Bose and Gupta (2020) based on detailed field and microstructural studies.
63 However, such variation in strain-rates can be present at any scale and thus, the order of
64 variation is especially important to understand whether the variation in strain-rates involved
65 simultaneously operating seismic and aseismic slip. The present study demonstrates a bimodal
66 grain size distribution of quartz in two adjacent mineralogically heterogeneous layers due to
67 partitioning of strain-rate at the microscopic scale in the mylonitized amphibolites along the
68 Karakoram Shear Zone (KSZ), India. The proportion of strain-rate partitioning has been
69 utilised to determine whether deformation occurred by seismic and/or aseismic slip in the two
70 adjacent layers. Based on the detailed microstructural observations, heterogeneous mineral
71 deformation behaviour along with a difference, between the two layers in terms of the strain-
72 rate accommodated per unit area has been inferred as the key factors for strain-rate

73 partitioning. Finally, implications of strain-rate partitioning in the middle-lower crust, for
74 variable offsets of streams and marker beds along widely-separated segments of the KSZ have
75 been discussed.

76 **2. Geological setting of the Karakoram Shear Zone**

77

78 The NW-SE trending dextral KSZ extends from Tash Gurgan in the northwest to Kailash
79 area in the southeast for a distance greater than 1000 km (Boutonnet et al., 2012; Molnar &
80 Tapponnier, 1978; Peltzer & Tapponnier, 1988; Robinson, 2009a; Searle et al., 1998;
81 Tapponnier et al., 1982; Valli et al., 2008; Weinberg et al., 2000; Weinberg et al., 2009; Wallis
82 et al., 2016). The KSZ lies in between the Shyok Suture zone (SSZ), to its southwest and the
83 Tibetan block, to its northeast (Figures 1a and 1b). The SSZ represents junction between
84 cretaceous Ladakh Batholith/arc and Tibetan margin that formed at ~85 Ma (Figure 1a;
85 Borneman et al., 2015; Pundir et al., 2020a). The KSZ is characterized by intensely deformed
86 and mylonitized granite gneisses, slates and sheared phyllites (Pundir et al., 2020a). The right
87 lateral motion along the KSZ is still supposed to be active along some of the segments as
88 reflected by the deflection in the course of the Indus River by 120 Km (Boutonnet et al., 2012;
89 Gaudemer et al., 1989; Robinson et al., 2015). However, there is a lot of debate on the active
90 portions of the fault and especially the rate of displacement along different segments and
91 therefore the offsets. For example, 120 Km (Phillips et al., 2004; Searle et al., 1998), 149-167
92 km (Robinson, 2009a), greater than 400 Km (Lacassin et al., 2004; Schwab et al., 2004; Valli
93 et al., 2008). Robinson (2009a) speculated that difficulties in estimation of long-term slip rates
94 could be due to dispute over initiation age and tectonic histories of the different segments of
95 the KSZ. This speculation becomes even more important in the light of granulite through
96 amphibolite to greenschist facies metamorphism, reported from different parts of the terrane
97 (Rolland et al., 2009).

Thus, apart from determining activity along specific segments of the KSZ in the present-day it is also important to characterize the ductile deformation underwent along the different segments of this zone during late Oligocene to mid-Miocene and more importantly the processes that operated during the deformation. Given this background, the present study documents micro-scale strain-rate partitioning in the mylonitized amphibolites across the Tangtse-Muglib mylonitic strands of the KSZ (Figure 1b; Borneman et al., 2015; Boutonnet et al., 2012; Boutonnet et al., 2013; Pundir et al., 2020a; 2020b; Searle et al., 1998; Searle and Philips, 2007; Sen et al., 2014; Wallis et al., 2016; Weinberg et al., 2000). It has been demonstrated that partitioning of strain-rate occurred between mineralogically distinct adjacent layers and the variable offsets along different segments of the KSZ can be manifestations of similar processes operating at various scales (micro- to- regional) in the present-day middle to lower crust.

3. Methodology

Major lithologies as well as the planar and linear structural fabrics in the Karakoram terrane were mapped mainly across the Tangtse-Muglib and the Darbuk-Shyok transects (Figure 1b), respectively. Oriented samples were collected from suitable outcrops and the planar and the linear structural data were plotted on Equal area projection diagrams. Oriented thin sections from the less-deformed as well as the mylonitized strands of the Karakoram Shear Zone (KSZ) were prepared from the oriented samples. The oriented thin sections were studied under a petrographic microscope and the major minerals were identified. Detailed microstructures of the major minerals were studied along with nature of deformation (rigid or plastic) of the different minerals along the KSZ. Recrystallization mechanism of quartz and feldspar were identified on the basis of microstructural criteria in accordance with Kruhl and Nega (1996), Stipp et al. (2002), Vernon (2004), Passchier and Trouw (2005) and Stipp et al. (2010). Based on these recrystallization mechanisms, the deformation temperatures were

123 estimated at previously estimated strain-rates of the order of 10^{-13} by Boutonnet et al. (2013)
 124 for the KSZ. Qualitative identification of high strain-rate micro-domains have been carried out
 125 on the basis of the proportion of nucleated recrystallized grains, the higher the proportion of
 126 recrystallized grains the higher is the strain-rate and vice-versa (Jia et al. 2009; Peternell et al.,
 127 2019). Moreover, Bose & Gupta (2020) correlated consistent increase in the proportion of
 128 dynamically recrystallized grains with an apparent reduction in competency contrast between
 129 feldspar and quartz which in turn was inferred as an outcome of increasing strain-rate by
 130 Vigneresse (2004). The positive correlation between strain rate and the proportion of
 131 dynamically recrystallized grains is also implied by the Orowan equation (Hull & Bacon,
 132 1986; Karato, 2008) which suggests that

$$133 \quad \dot{\epsilon} = b\rho v, \quad (1)$$

134 where, $\dot{\epsilon}$ is the strain-rate, b is the burgers vector, ρ is the dislocation density and v is the
 135 dislocation velocity. This implies that in the absence of considerable strain-hardening (ρ does
 136 not vary significantly with strain rate) extent of dislocation creep increases with strain rate; a
 137 greater extent of dislocation creep is manifested in a higher proportion of dynamically
 138 recrystallized grains (Tullis et al., 2000; Vernon, 2004). Thus, in the absence of considerable
 139 strain-hardening, zones with a higher proportion of dynamically recrystallized grains can be
 140 correlated with higher strain rates (Jia et al., 2019), while lower strain rate zones are
 141 characterized by a higher proportion of relict (non-recrystallized) clasts. The ratio of the strain-
 142 rates between two micro-domains has been calculated using a combination of the ductile
 143 rheological law (Gleason & Tullis, 1995) and the different piezometers of Twiss (1977), Stipp
 144 & Tullis (2003) and Shimizu (2008). The strain accommodated by a particular micro-domain
 145 has been calculated by multiplying the strain-rate with the duration of deformation and has
 146 been converted into displacement using the equation of Fagereng and Biggs, 2019:

$$147 \quad \gamma = d/w \quad (2)$$

where, γ is the shear strain, d is the displacement parallel to the boundaries of the zone that had undergone shear deformation at a particular rate and w is the width of the zone that had been deformed during shearing.

Based on the above methods, micro-scale partitioning of strain-rate has been demonstrated between two adjacent micro-domains which can be used to explain aseismic strain localization in outcrop as well as in regional scale.

4. Results

4.1. Lithology and structure

Major lithounits exposed along the Tangtse-Muglib strand include mylonitised amphibolites and granite gneisses (Figure 2a). The mylonitic foliation strikes NW-SE (Figures 1b & 2b) and dips steeply either towards NE or SW (Figure 1b). Granite gneisses, in contact with the amphibolites preserve a prominent segregation between the feldspathic and the quartz-rich layers (Figure 2b). The feldspathic layers, generally pinch out within the apparently less competent quartz-rich layers (Figure 2b) and exhibit a prominent dextral asymmetry in plan (Figure 2b). On the surface of the mylonitic foliation (S; Figures 2c & d) a subhorizontal stretching lineation (L) is detected (Figures 2c & d) which is conformable with the observed dextral asymmetry (Figure 1b) in plan.

4.2. Microstructure

4.2.1. Granite gneisses

The mylonitic foliation in the granite gneisses (location TM 1 in Figure 1b) is defined by an alternate segregation between feldspathic and quartz-rich layers as also observed on ground (Figure 2b). Both these layers are essentially monomineralic in nature (Figure 3a) with sharp distinct boundaries between the two and is devoid of any cusps and lobes or interfingering along the boundaries (Figure 3a). Within the quartz-rich layers interfingering is observed along amoeboid grain boundaries (Figure 3b) that exhibit sutures with wavelengths of the order of the grain size (Kruhl & Nega, 1998; Vernon, 2004) implying pre-dominant GBM recrystallization (Stipp et al., 2002; Vernon, 2004). Lack of any layered arrangement of uniform-sized recrystallized grains precludes the possibility of significant recrystallisation by subgrain rotation (SGR; Stipp et al., 2002), at least in the studied lithounits. This implies that deformation temperature was above ~550 °C (Stipp et al., 2002) if conventional strain rates (Pfiffner & Ramsay, 1982; Law, 2014) are assumed. On the other hand, in the feldspathic domains core-mantle structures (Figure 3c) are observed with a mantle of recrystallized grains surrounding relict feldspar cores (Figure 3c). Sharp, distinct boundaries between the core and the recrystallized mantle (Figure 3c) suggest that the feldspars underwent recrystallization by bulging (BLG) mechanism that occurs at temperatures, not more than ~600 °C. Thus, microstructural studies carried out on the mylonitic fabric-defining minerals i.e., feldspar and quartz reveal prevailing temperatures in between ~550-600 °C during the dextral shearing event. Importantly, Boutonnet et al. (2013) calculated strain rates of the order of 10^{-13} s^{-1} by applying quartz-strain-rate-metry (QSR) on the lithounits deformed along the mylonitic strands of the KSZ.

4.2.2. Mylonitized amphibolites

In the relatively low strain zones (locations DS6-DS8 in Fig. 1b), the foliation is defined by a preferred orientation of biotite (Figures 3d & 3e) and quartz ribbons (Figure 3e). Within the quartz ribbons, grain boundaries of quartz exhibit amoeboid sutures (Figure 3e) with

wavelengths of the order of the grain-size. This implies that quartz grains recrystallized by grain boundary migration (GBM), similar to that in the granite gneisses. Importantly, the amphiboles do not show any considerable preferred orientation (Figures 3d-3f) in these low strain zones, unlike the biotites, and appear to have deformed by fracturing and rotation of mechanical fragments. Deformed lamellar twins or wedge twins are observed in plagioclase feldspar.

The mylonitized amphibolites (location TM 2 in Fig. 1b; Figures 2a & 2d), in contact with the granite gneisses along the mylonitic strands of the KSZ, preserve the mylonitic foliation (concordant with that in the gneisses) along with a subhorizontal stretching lineation on the foliation (Figure 2d). Therefore, in all probability, the amphibolites were also subjected to dextral shearing along with the granite gneisses at ~550-600 °C. Within the mylonitized amphibolites, quartz grains exhibit an approximate bimodal grain-size distribution (Figures 4a-4d) with coarser-grained monomineralic quartz-rich layers (CGQL; Figures 4a-4f) and finer-grained quartz-amphibole-biotite rich layers (AMBIORL; Figures 4a-4d & 4f). Coarser quartz grains in the monomineralic layers with very few amphiboles and biotite grains (Figures 4b & d-f) have amoeboid boundaries with interfingering contacts (Figures 4e & 4f). Sutures along the boundaries have wavelengths of the order of the grain size, implying GBM as the recrystallization mechanism in quartz, similar to that in the lower strain zones and the granite gneisses (Figure 3b). However, a significant reduction in grain size of quartz is observed in the fine-grained layers (Figures 4a-4d & 4f), which also contain a considerable proportion of amphibole and biotite (Figures 4a-d & 4f). This significant reduction in grain size implies a higher rate of nucleation of quartz in the fine-grained layers, which might result from a greater extent of dynamic recrystallization of quartz. This proposition becomes even more evident as ribbons of quartz, sandwiched between amphiboles and biotites, are also detected in the fine-grained layers (Figures 4b & 4f). As the

temperature of deformation did not exceed ~600 °C, pinning of quartz by amphibole and biotite in the fine-grained layers is manifested in the form of quartz grains with straight grain boundaries at high angles to the foliation, occurring within the ribbons (Figures 4b, 4d & 4f). Nevertheless, the grain sizes in the finer-grained layers appear to be the characteristic of bulging recrystallization mechanism (BLG; Stipp et al., 2002; 2010), although no preserved evidence of BLG mechanism (bulges with wavelengths of an order significantly lower than that of the grain-size) have been detected (Figures 3 & 4). Moreover, in the coarser-grained layers, quartz-grains indicate recrystallization by GBM. These layers do not apparently preserve deformation bands and sub-grain boundaries, which generally indicate a higher internal strain within the individual grains. This is in disagreement with BLG mechanism that is much more likely to be associated with micro-domains in which quartz grains preserve a higher internal strain, at least under conventional strain rates (Pfiffner & Ramsay, 1982), similar to the prevalent conditions (strain rate $\sim 10^{-13} \text{ s}^{-1}$; Boutonnet et al., 2013) in the present case. Even within the fine-grained layers, there is variation in grain-size with relatively finer grains adjacent to microdomains with a higher modal proportion of amphibole and biotite and vice versa (Figures 4c, 4d & 4f). Thus, the extent of nucleation of quartz grains appears to be related somehow to the proportion of amphiboles and biotites.

5. Discussion

Mylonitized amphibolites and granite gneisses, exposed along the Tangtse-Muglib strands of the dextral KSZ, underwent deformation at ~550-600 °C under conventional strain rates. The amphiboles and the biotites in the amphibolites had a tendency to segregate into layers alternating with coarser-grained, monomineralic quartz-rich domains with increasing strain during dextral shearing. Within the amphibole-biotite-rich layers (AMBIORL) in the mylonitized amphibolites, the quartz grains are significantly finer than those in the monomineralic coarse-grained quartz-rich layers (CGQL). This can be either due to the

recrystallization of quartz by BLG (Stipp et al., 2002; 2010) in the AMBIORL and/or considerably greater grain nucleation during dynamic recrystallization than that in the CGQL. Other than the grain size of quartz, the AMBIORL and the CGQL also differ in the modal proportion of amphiboles and biotites. Therefore, it becomes important to investigate the mechanism of fining of quartz grains in the AMBIORL to determine whether the fining is related to the higher modal proportion of amphiboles and biotites.

5.1. Finer quartz in the AMBIORL: BLG or higher grain-nucleation rate?

The gross grain size of quartz in the fine-grained layers (AMBIORL) is similar to the size of those grains, which reportedly forms during BLG recrystallization of quartz (Figures 4b & d; Stipp et al., 2002; 2010). However, the absence of any crosscutting relationship between the AMBIORL and the CGQL (Figure 4), along with the parallelism of these two layers (Figure 4), suggests that both these layers deformed simultaneously. Apart from this, the granite gneisses in contact with the mylonitized amphibolites do not preserve any evidence of BLG recrystallization, although the mesoscopic mylonitic foliation in the two lithologies is in concordance with each other. Microstructural features of feldspar and quartz in both the lithologies undoubtedly indicate deformation temperatures to ~550-600 °C. Therefore, it is very much unlikely that even if BLG operated in quartz in the AMBIORL, locally in microscopic scale, it was not associated with deformation temperatures of ~280-400 °C (Stipp et al., 2002) at which BLG in quartz generally operates under conventional strain rates (Figure 5; Stipp et al., 2002; 2010). Moreover, the prevalence of ~280-400 °C temperatures is difficult to visualize exclusively in the AMBIORL, which does not show any crosscutting relationship with the mesoscopic foliation and the CGQL and especially when GBM, in general, is the pre-dominant recrystallization mechanism in quartz. Thus, BLG, if occurred at all, must have operated under strain rates of 10^{-8} to 10^{-9} s^{-1} (Figure 5), which is at least about 10^4 to 10^5 times higher than the conventional strain rates (Pfiffner &

271 Ramsay, 1982) at 550-600 °C (Fig. 5). On the contrary, theoretical estimates using Fig. 5
272 suggest that GBM in the coarse-grained layers could not have operated at strain rates higher
273 than about 10^{-11} s^{-1} at 550-600 °C (Figure 5). Based on QSR, Boutonnet et al. (2013)
274 inferred strain rates greater than $1.6 \times 10^{-13} \text{ s}^{-1}$ along the mylonitic strands of the KSZ.
275 Therefore, based on a combination of the strain rate data of Boutonnet et al. (2013) and
276 undoubted evidence of GBM recrystallization in quartz, the strain-rate in the CGQL can be
277 constrained in the range of 1.6×10^{-13} to 10^{-11} s^{-1} at 550-600 °C (Figure 5; Boutonnet et
278 al., 2013). Thus, if BLG and GBM in quartz operated simultaneously in the AMBIORL and
279 the CGQL, respectively, then quartz in the AMBIORL must have deformed at a rate of about
280 10^2 to 10^5 times higher than the quartz in the CGQL (Figure 5). In this context, the higher
281 nucleation of quartz grains in the AMBIORL can be attributed to a higher rate of dynamic
282 recrystallization in the AMBIORL than in the CGQL. Nucleation of grains during
283 deformation is often positively correlated with strain rate (Paternell et al., 2019; Jia et al.,
284 2009), i.e., a higher strain-rate will lead to an increase in the nucleation of grains, as also
285 inferred quantitatively by the experimental studies of Paternell et al. (2009). Bose and Gupta
286 (2020) systematically correlated a higher proportion of recrystallized feldspar and quartz with
287 a consistent apparent reduction in competency-contrast between these two minerals, which in
288 turn indicates a higher strain-rate by the global model of Vigneresse (2004). Therefore, in the
289 absence of significant strain hardening in the quartz grains, the proportion of nucleated
290 dynamically recrystallized grains is likely to increase with an increase in strain rate. Thus, a
291 difference exists in the rate of deformation of quartz between the CGQL and the AMBIORL.
292 In other words, irrespective of the operation of BLG and/or higher grain nucleation rate (than
293 the CGQL) in the AMBIORL, strain-rate partitioning occurred between the CGQL and the
294 AMBIORL on the microscopic scale. However, it is yet to be determined, whether the

proportion of strain-rate partitioning was sufficient to cause simultaneous operation of GBM and BLG in the quartz grains in the CGQL and the AMBIORL, respectively.

5.2. Proportion of partitioning of strain-rate between CGQL and AMBIORL

Although strain-rate partitioning in between the CGQL and the AMBIORL becomes evident from the discussions above, the proportion in which the partitioning occurred is yet to be understood. Determination of the proportion of strain-rate partitioning can have implications for simultaneous seismic and/or aseismic slip partitioning in micro-scale. We assessed the proportion of partitioning of strain-rate between the CGQL and the AMBIORL using a combination of the ductile rheological law (Gleason & Tullis, 1995) and the piezometric equations (Shimizu, 2008; Stipp & Tullis, 2003; Twiss, 1977). The ductile rheological law has been used in accordance with the formulation of Gleason and Tullis (1995) as follows:

$$\dot{\epsilon} = d\epsilon/dt = A \cdot \sigma^n \cdot e^{-Q/RT} \quad (3)$$

Where Q is the activation energy, A is a material parameter, R is the ideal gas constant, T is the temperature, σ is the flow stress, and n , the stress exponent = 4 (derived experimentally).

Piezometric equations applied in calculation include:

$$\sigma = K_{(Twiss, 1977)} \cdot D^{-0.68}; \text{ after Twiss (1977);}$$

where, $K_{(Twiss, 1977)}$ is the constant in the piezometric equation of Twiss (1977)

$$\sigma = K_{(Stipp \text{ and } Tullis, 2003)} \cdot D^{-0.794}; \text{ after Stipp and Tullis (2003)}$$

where, $K_{(Stipp \text{ and } Tullis, 2003)}$ is the constant in the piezometric equation of Stipp and Tullis (2003)

$$\sigma = K_{(Shimizu, 2008)} \cdot D^{-0.8}; \text{ after Shimizu (2003)}$$

317 where, $K_{(Shimizu, 2008)}$ is the constant in the piezometric equation of Shimizu (2008)

318 The mean grain size (D; Table 1) has been calculated based on optical studies and as
319 per the formulations of Christie and Ord (1980).

320 For the CGQL, combination of ductile rheological law and piezometric equations yields

321 $\dot{\epsilon} = A. K_{(Twiss, 1977)} \cdot (4.64 \times 10^{-3}) \cdot e^{-QRT}; \sigma$ substituted after Twiss (1977) (7)

322 $\dot{\epsilon} = A. K_{(Stipp and Tullis, 2003)} \cdot (1.87 \times 10^{-3}) e^{-QRT}; \sigma$ substituted after Stipp and Tullis
323 (2003)

324 (8)

325 $\dot{\epsilon} = A. K_{(Shimizu, 2008)} \cdot (1.66 \times 10^{-3}) e^{-QRT}; \sigma$ substituted after Shimizu (2008) (9)

326

327 For the AMBIORL, combination of ductile rheological law and piezometric equations yields

328 $\dot{\epsilon} = A. K_{(Twiss, 1977)} \cdot (1.085 \times 10^{-2}) e^{-QRT}; \sigma$ substituted after Twiss (1977) (10)

329 $\dot{\epsilon} = A. K_{(Stipp and Tullis, 2003)} \cdot (6.27 \times 10^{-3}) e^{-QRT}; \sigma$ substituted after Stipp and Tullis
330 (2003)

331 (11)

332 $\dot{\epsilon} = A. K_{(Shimizu, 2008)} \cdot (5.69 \times 10^{-3}) e^{-QRT}; \sigma$ substituted after Shimizu (2008) (12)

333 Based on these equations (7-12), it has been estimated that quartz in the AMBIORL
334 deformed at a rate 2.34-3.43 times higher than that in the CGQL as per the following
335 calculations:

336 $\dot{\epsilon}_{AMBIORL} / \dot{\epsilon}_{CGQL} = (1.085 \times 10^{-2}) / (4.64 \times 10^{-3});$ dividing equation (10) by equation (7)

$$= 2.34 \quad (13)$$

338

$$\dot{\epsilon}_{AMBIORL}/\dot{\epsilon}_{CGQL} = (6.27 \times 10^{-3}) / (1.87 \times 10^{-3}); \text{ dividing equation (11) by equation (8)}$$

$$= 3.35 \quad (14)$$

$$\dot{\epsilon}_{AMBIORL}/\dot{\epsilon}_{CGQL} = (5.69 \times 10^{-3}) / (1.66 \times 10^{-3}) ; \text{ dividing equation (12) by equation (9)}$$

$$= 3.43 \quad (15)$$

343 Therefore, the partitioning of strain-rate in the AMBIORL is about $10^0 - 10^1$ times
 344 higher than that in the CGQL. Thus, it can be inferred that the finer grain-size of quartz in the
 345 AMBIORL was solely due to micro-scale strain-rate partitioning and not due to any BLG
 346 recrystallization mechanism that, on the other hand, would require the quartz in the
 347 AMBIORL to deform at a rate 10^2 to 10^5 times higher than the quartz in the CGQL, as
 348 discussed in section 4.1. Moreover, as the AMBIORL deformed at a rate, 2.34-3.43 times
 349 higher than the CGQL then displacement accomdated in 12 Ma (duration of shearing along
 350 the KSZ as per Pundir et al., 2020b) by the AMBIORL and the CGQL is 0.92 cm and 2.79-
 351 4.1 cm (see Appendix), respectively. This displacement values imply extremely slow slip as
 352 categorized by Nielsen (2017). Therefore, neither of the two layers deformed at high strain
 353 rates and were involved in any seismic slip that is generally associated with velocities in the
 354 order of ms^{-1} (Nielsen, 2017) and strain-rates of $1 to 10^2 s^{-1}$ (Kreemer et al., 2014;
 355 Fagereng and Biggs, 2019). Thus, partitioning of strain-rate at the microscopic scale between
 356 the CGQL and the AMBIORL, was associated with extremely slow slip deformation by
 357 aseismic creep in both the layers. In accordance with observations and calculations, slow
 358 aseismic creep was more localized in the AMBIORL than in the CGQL. So, strain-rate

partitioning can be a very common mechanism for strain localization during aseismic creep across any scale especially in the presence of mineralogical and lithological heterogeneities.

5.3. Partitioning of strain-rate: why and how?

At temperatures of 550-600 °C, although feldspar and quartz can undergo deformation by dislocation creep, amphibole is more likely to deform by fracturing and mechanical rotation due to its reported brittle-ductile transition at least above 700 °C (Passchier & Trouw, 2005). For example, Ross and Wilks (1996) inferred simultaneous plastic deformation of plagioclase by dislocation creep and fracturing and mechanical rotation of fragments of hornblende. Nevertheless, the preferred orientation of amphiboles in the high strain zones (Figures 4b-4d), unlike in the relatively lower strain zones (Figures 3d; Figure 6a), suggests that the amphiboles underwent rigid rotation towards the finite extension direction in the high strain zones (Figures 6b-6c). Fracturing in amphiboles could have also occurred under conditions when the applied stress exceeded the yield strength of amphiboles. On the other hand, Biotites deformed plastically with ease at ~550-600 °C as the brittle-ductile transition for biotite occurs at temperatures as low as 150-250 °C (Passchier & Trouw, 2005). However, biotite can deform only by slip on the basal plane along the $\langle 100 \rangle$ and the $\langle 110 \rangle$ directions (Passchier & Trow, 2005). In this context, it is noteworthy that biotite belongs to the monoclinic crystal system, with very few symmetry elements. As a result, plastic deformation of biotite can occur by slip on only one suitably oriented slip plane along very few slip directions, unlike quartz, which, due to the presence of a larger number of symmetry elements (trigonal or hexagonal crystal system), can accommodate deformation by slip along any of the six $\langle a \rangle$ directions on several crystallographic planes (Abalos et al., 2016; Hobbs, 1985; Mainprice et al., 1986; Schmid and Casey, 1986; Twiss and Moores, 1992). Thus, although biotite in the AMBIORL underwent plastic deformation during shearing along the KSZ, the availability of very few slip systems may well have restricted the biotites from

accommodating the bulk of the strain. Under this situation, the bulk of the strain in the AMBIORL was undoubtedly partitioned into the quartz-bearing domains (adjacent to amphiboles and biotites), especially at temperatures where quartz can deform easily by slip along any of the a-axes on several crystallographic planes.

Summarising the above facts, in the low strain zones of the KSZ, the foliation in the amphibolites is defined mainly by a preferred orientation of biotites, and amphiboles do not show any significant alignment (Figure 6a). The amphiboles and biotites were segregated into distinct micro-domains with increasing strain (AMBIORL in Figure 6b). The bulk of the strain on the AMBIORL was localized into the quartz-bearing domains (Figure 6b) as amphiboles did not undergo ductile deformation, and the biotites accommodated limited strain. The occurrence of amphiboles and biotites in the AMBIORL, resulted in (a) the localization of strain in the quartz-rich domains of the AMBIORL with strain on the quartz grains naturally decreasing with distance from the amphiboles and biotites and (b) effective reduction of the areal proportion of quartz in any particular area (e.g., A in Figure 6b) in the AMBIORL than that in a similar area (A) in the CGQL (Figure 6b).

Thus, strain accommodated per unit area over any time interval (t) by quartz in the AMBIORL will be higher than the strain per unit area on the quartz over the same time interval (t) in the CGQL. As a result, the rate of deformation of quartz in the AMBIORL must have been higher than that in the CGQL. A higher deformation rate in the AMBIORL resulted in higher nucleation of dynamically recrystallized grains in the AMBIORL than in the CGQL (Figure 6c).

5.4. Implications of strain-rate partitioning for the KSZ

407 Micro-scale partitioning of strain-rate as discussed above for the mylonitized
408 amphibolites along the Tangtse-Muglib strand of the KSZ is promoted by an increase in
409 mineralogical and, therefore, rheological heterogeneity as demonstrated in section 5.3.
410 Considering that the KSZ deformed continuously from ~27-15 Ma (Pundir et al., 2020b), at a
411 bulk strain rate of $1.6 \times 10^{-13} \text{ s}^{-1}$ (Boutonnet et al., 2013), a bulk strain of 60.5 and 141.6-
412 207.5 (see Appendix) were accommodated by the CGQL and the AMBIORL, respectively, in
413 the mylonitized amphibolites. For orthogonal thicknesses of $w = 152.3 \text{ } \mu\text{m}$ and $w' = 197.1$
414 μm (Figure 4d; Fig. 7a), for example, for the CGQL and the AMBIORL, respectively,
415 displacement accommodated by the CGQL will be 0.92 cm (Fig. 7a; see Appendix), whereas
416 in the AMBIORL will accommodate a displacement of 2.79-4.1 cm (Figure 7a, see
417 Appendix), as per equation (2). Therefore, even in the scale of a thin section, displacement
418 accommodated by the AMBIORL will be 1.87-3.18 cm greater than that accommodated by
419 the CGQL ((see Appendix; Figure 7a). If a similar proportion of strain-rate partitioning and
420 hence the accommodated strain are extrapolated to two adjacent deformed hypothetical
421 layers, each 10 meters thick (outcrop scale; Figure 7b), then displacement in layer 2 that
422 accommodated higher bulk strain will be about 800-1500 meters greater than that in the less
423 deformed layer 1 (Figure 7b, see Appendix). If similar extrapolation is done on two adjacent
424 hypothetical layers, each 1.25 km thick (Figure 7c; regional scale; total thickness 2.5 km
425 similar to the width of the Tangtse strand in Figure 1b), then layer 2 (more deformed) will
426 accommodate a displacement of about 100-200 km greater than that accommodated by the
427 less-deformed layer 1 (Figure 7c, see Appendix). It is noteworthy that the calculations for
428 Figures 7b and 7c are based on hypothetical layers between which strain-rate has been
429 assumed to have partitioned in a proportion similar to that between the AMBIORL and the
430 CGQL. Therefore, the calculated displacement should not supposedly represent the actual
431 displacement along the Tangtse strand of the KSZ (Figure 1b). Nevertheless, variations in

offsets, similar to that calculated in Figure 7c, are observed along widely separated segments of the KSZ (Robinson, 2009a). Therefore, the calculations using hypothetical layers in Figures 7b & 7c has just been carried out to assess an estimate of the order of difference in displacements accommodated by any two mineralogically and/or lithologically and hence rheologically distinct layers between which strain-rate has been partitioned at a given proportion. Thus, considering the natural lithological and hence rheological heterogeneity across the shear zone on a regional scale, significant differences in accommodated displacement between two adjacent layers are bound to occur even along any single segment of the approximately 1000 km long KSZ. This implies that the displacements along widely dispersed segments of the KSZ are likely to vary significantly, which is actually the case (Robinson, 2009b). Presently and also in the Quaternary, ductile deformation at mid-crustal depths of the lithospheric scale KSZ (Paul et al., 2021) must have involved similar strain-rate partitioning across diverse scales which might very well be responsible for the observed differences in offsets of marker beds and streams across the widely separated segments of the shear (Lacassin et al., 2004; Phillips et al., 2004; Robinson, 2009a; Schwab et al., 2004; Searle et al., 1998; Valli et al., 2008).

6. Conclusion

During ductile deformation, rigid minerals incapable of ductile flow and minerals that undergo limited plastic deformation can lead to micro-scale partitioning of the rate of deformation of the mineral that can easily undergo plastic deformation. Partitioning of strain-rate along natural shear zones is promoted by increasing mineralogical, lithological, and therefore rheological heterogeneities, which leads to the accommodation of strain at a higher

rate in the heterogeneous layers. Therefore, a higher strain accommodation occurs over a particular lateral distance across any shear zone.

Partitioning of strain-rate in between the CGQL and the AMBIORL in the mylonitized amphibolites along the KSZ involved slow aseismic creep and was not associated with any fast-slip seismic events. Thus, strain-rate partitioning appears as an important mechanism of strain localization during aseismic creep.

In the context of the KSZ, strain-rate partitioning between mineralogically heterogeneous layers of the same lithology and between different lithologies can account for variable displacement even across any single segment of the shear. Thus, KSZ, being a 1000 km long lithospheric shear zone, must have transected different lithologies and hence different rheologies in the vertical and horizontal directions due to which variability in displacement along different segments of the shear appears to be a natural phenomenon. Similar processes must have occurred at middle to lower crustal depths, along and across the lithospheric KSZ, from Quarternary to the present. The manifestations of the variation in displacements in the ductile regime can very well be the variable offsets of marker beds and streams across the Karakoram Fault, now observed on the surface.

Acknowledgements

Data used in this study is available in Mendeley Data, Version 1, doi: 10.17632/rzjphcs8v7.1, (<https://data.mendeley.com/datasets/rzjphcs8v7/1>). This work was supported by Science and Engineering Research Board grant EMR/2014/000555 and Wadia Institute of Himalayan Geology grant Activity 7c of CAP-Himalaya awarded to Vikas Adlakha. Manoranjan Mohanty and Rajwant of Department of Science and Technology (DST) and Science and Engineering Research Board (SERB), New Delhi, respectively, are thanked for their continuous support and encouragement. Discussions with Koushik Sen improved the paper.

Chhutapa Phuntsog Dorjay, Skalzang Namgyal, and Thinless Gyachho are thanked for field assistance. The Indo-Tibetan Border Police (ITBP) is highly acknowledged for help during fieldwork in the Ladakh, NW India. We also thank Saibal Gupta of IIT Kharagpur, Ramesh Chandra Patel of BHU Varanasi and Director, WIHG for encouragement.

References

- Ábalos, B., Puelles, P., Fernández-Armas, S., & Sarrionandia, F. (2011). EBSD microfabric study of pre-Cambrian deformations recorded in quartz pebbles from the Sierra de la Demanda (N Spain). *Journal of Structural Geology*, 33(4), 500-518.
<https://doi.org/10.1016/j.jsg.2011.01.005>
- Borneman, N.L., Hodges, K.V., Van Soest, M.C., Bohon, W., Wartho, J.A., Cronk, S.S., Ahmad, T. (2015). Age and structure of the Shyok suture in the Ladakh region of northwestern India: Implications for slip on the Karakoram fault system. *Tectonics*, 34(10), 2011-2033. <https://doi.org/10.1002/2015TC003933>
- Bose, S., & Gupta, S. (2020). Evolution of stretching lineations in granulite-hosted ductile shear zones, Eastern Ghats Province, India: Role of temperature, strain rate and pre-existing stretching lineations. *Journal of Structural Geology*, 138, 104127.
<https://doi.org/10.1016/j.jsg.2020.104127>
- Boutonnet, E., Leloup, P.H., Arnaud, N., Paquette, J.L., Davis, W.J., & Hattori, K. (2012). Synkinematic magmatism, heterogeneous deformation, and progressive strain localization in a strike-slip shear zone: The case of the right-lateral Karakorum fault. *Tectonics*, 31(4). <https://doi.org/10.1029/2011TC003049>

- Boutonnet, E., Leloup, P.H., Sassier, C., Gardien, V., & Ricard, Y. (2013). Ductile strain rate measurements document long-term strain localization in the continental crust. *Geology*, 41(8), 819-822. <https://doi.org/10.1130/G33723.1>
- Cannon, J.M., Murphy, M.A., & Taylor, M. (2018). Segmented strain accumulation in the High Himalaya expressed in river channel steepness. *Geosphere*, 14(3), 1131–1149. <https://doi.org/10.1130/GES01508.1>
- Christie, J.M., & Ord, A. (1980). Flow stress from microstructures of mylonites: example and current assessment. *Journal of Geophysical Research: Solid Earth*, 85(B11), 6253-6262. <https://doi.org/10.1029/JB085iB11p06253>
- Fagereng, Å., & Biggs, J. (2019). New perspectives on ‘geological strain rates’ calculated from both naturally deformed and actively deforming rocks. *Journal of Structural Geology*, 125, 100-110. <https://doi.org/10.1016/j.jsg.2018.10.004>
- Fan, S., & Murphy, M.A. (2021). Three-dimensional strain accumulation and partitioning in an arcuate orogenic wedge: An example from the Himalaya. *Geological Society of America Bulletin*, 133(1-2), 3-18. <https://doi.org/10.1130/B35528.1>
- Gahalaut, V.K., Kundu, B., Laishram, S.S., Catherine, J., Kumar, A., Singh, M.D., Tiwari, R.P., Chadha, R.K., Samanta, S.K., Ambikapathy, A., & Mahesh, P. (2013). Aseismic plate boundary in the Indo-Burmese wedge, northwest Sunda Arc. *Geology*, 41(2), 235-238. <https://doi.org/10.1130/G33771.1>
- Gaudemer, Y., Tapponnier, P., & Turcotte, D.L. (1989). River offsets across active strike-slip faults.
- Gleason, G.C., & Tullis, J. (1995). A flow law for dislocation creep of quartz aggregates determined with the molten salt cell. *Tectonophysics*, 247(1-4), 1-23. [https://doi.org/10.1016/0040-1951\(95\)00011-B](https://doi.org/10.1016/0040-1951(95)00011-B)

525 Hirth, G., & Tullis, J.A.N. (1992). Dislocation creep regimes in quartz aggregates. *Journal of*
526 *Structural Geology*, 14(2), 145-159. [https://doi.org/10.1016/0191-8141\(92\)90053-Y](https://doi.org/10.1016/0191-8141(92)90053-Y)

527 Hobbs, B.E. (1985). The hydrolytic weakening effect in quartz. *Point Defects in Minerals*,
528 31, 151-170. <https://doi.org/10.1029/GM031p0151>

529 Hull, D., & Bacon, D.J. (2001). *Introduction to dislocations*. Butterworth-Heinemann.

530

531 Ji, S. (1998). Deformation Microstructure of Natural Plagioclase. In *Fault-related Rocks* (pp.
532 276-277). Princeton University Press. <https://doi.org/10.1515/9781400864935.276>

533 Jia, Z., Gao, Z., Ji, J., Liu, D., Guo, T., & Ding, Y. (2019). Study of the dynamic
534 recrystallization process of the Inconel625 alloy at a high strain rate. *Materials*,
535 12(3), 510. <https://doi.org/10.3390/ma12030510>

536 Karato, S. (2008). *Deformation of Earth Materials*. Cambridge University Press, Cambridge.

537 Kreemer, C., Blewitt, G., & Klein, E.C. (2014). A geodetic plate motion and Global Strain
538 Rate Model. *Geochemistry, Geophysics, Geosystems*, 15(10), 3849-3889.
539 <https://doi.org/10.1002/2014GC005407>

540 Kruhl, J.H., & Nega, M. (1996). The fractal shape of sutured quartz grain boundaries:
541 application as a geothermometer. *Geologische Rundschau*, 85(1), 38-43.

542 Lacassin, R., Valli, F., Arnaud, N., Leloup, P.H., Paquette, J.L., Haibing, L., Tapponnier, P.,
543 Chevalier, M.L., Guillot, S., Maheo, G., Zhiqin, X. (2004). Large-scale geometry,
544 offset and kinematic evolution of the Karakorum fault, Tibet. *Earth and Planetary*
545 *Science Letters*, 219(3-4), 255-269. [https://doi.org/10.1016/S0012-821X\(04\)00006-8](https://doi.org/10.1016/S0012-821X(04)00006-8)

546 Law, R.D. (2014). Deformation thermometry based on quartz c-axis fabrics and
547 recrystallization microstructures: A review. *Journal of Structural Geology*, 66, 129-
548 161. <https://doi.org/10.1016/j.jsg.2014.05.023>

549 Mainprice, D., Bouchez, J.L., Blumenfeld, P., & Tubià, J.M. (1986). Dominant c slip in
 550 naturally deformed quartz: Implications for dramatic plastic softening at high
 551 temperature. *Geology*, 14(10), 819-822. [https://doi.org/10.1130/0091-
 552 7613\(1986\)14<819:DCSIND>2.0.CO;2](https://doi.org/10.1130/0091-7613(1986)14<819:DCSIND>2.0.CO;2)
 553 Molnar, P., & Tapponnier, P. (1978). Active tectonics of Tibet. *Journal of Geophysical
 554 Research: Solid Earth*, 83(B11), 5361-5375. <https://doi.org/10.1029/JB083iB11p05361>
 555 Nielsen, S. (2017). From slow to fast faulting: recent challenges in earthquake fault
 556 mechanics. *Philosophical Transactions Royal Society A* 375: 20160016.
 557 <http://dx.doi.org/10.1098/rsta.2016.0016>
 558 Ojo, A.O., Kao, H., Jiang, Y., Craymer, M., & Henton, J. (2021). Strain Accumulation and
 559 Release Rate in Canada: Implications for Long-Term Crustal Deformation and
 560 Earthquake Hazards. *Journal of Geophysical Research Solid Earth*.
 561 <https://doi.org/10.1029/2020JB020529>
 562 Panda, D., Kundu, B., Gahalaut, V.K., & Rangan, C. (2020). India-Sunda plate motion,
 563 crustal deformation, and seismic hazard in the Indo-Burmese Arc. *Tectonics*, 39(8),
 564 p.e2019TC006034. <https://doi.org/10.1029/2019TC006034>
 565 Passchier, C.W., & Trouw, R.A. (2005). *Microtectonics*. Springer Science & Business Media.
 566 Paul, A., Hazarika, D., Wadhawan, M., & Kumar, N. (2021). Upper mantle anisotropy in the
 567 northwest Himalaya and Ladakh-Karakoram zone based on SKS splitting analysis.
 568 *Journal of Geodynamics*, 144, 101817. <https://doi.org/10.1016/j.jog.2021.101817>
 569 Peltzer, G., & Tapponnier, P. (1988). Formation and evolution of strike-slip faults, rifts, and
 570 basins during the India-Asia collision: An experimental approach. *Journal of
 571 Geophysical Research: Solid Earth*, 93(B12), 15085-15117.
 572 <https://doi.org/10.1029/JB093iB12p15085>

573 Paternell, M., Wilson, C.J., & Hammes, D.M. (2019). Strain rate dependence for evolution
 574 of steady state grain sizes: Insights from high-strain experiments on ice. *Earth and*
 575 *Planetary Science Letters*, 506, 168-174. <https://doi.org/10.1016/j.epsl.2018.10.037>
 576 Pfiffner, O.A., & Ramsay, J.G. (1982). Constraints on geological strain rates: arguments from
 577 finite strain states of naturally deformed rocks. *Journal of Geophysical Research:*
 578 *Solid Earth*, 87(B1), 311-321. <https://doi.org/10.1029/JB087iB01p00311>
 579 Phillips, R.J., Parrish, R.R., & Searle, M.P. (2004). Age constraints on ductile deformation
 580 and long-term slip rates along the Karakoram fault zone, Ladakh. *Earth and*
 581 *Planetary Science Letters*, 226(3-4), 305-319.
 582 <https://doi.org/10.1016/j.epsl.2004.07.037>
 583 Pryer, L.L. (1993). Microstructures in feldspars from a major crustal thrust zone: the
 584 Grenville Front, Ontario, Canada. *Journal of structural Geology*, 15(1), 21-36.
 585 [https://doi.org/10.1016/0191-8141\(93\)90076-M](https://doi.org/10.1016/0191-8141(93)90076-M)
 586 Pundir, S., Adlakha, V., Kumar, S., & Singhal, S. (2020a). Closure of India–Asia collision
 587 margin along the Shyok Suture Zone in the eastern Karakoram: new geochemical and
 588 zircon U–Pb geochronological observations. *Geological Magazine*, 157(9), 1451-
 589 1472. <https://doi.org/10.1017/S0016756819001547>
 590 Pundir, S., Adlakha, V., Kumar, S., Singhal, S., & Sen, K. (2020b). Petrology, geochemistry
 591 and geochronology of granites and granite gneisses in the SE Karakoram, India:
 592 Record of subduction-related and pre-to syn-kinematic magmatism in the Karakoram
 593 Fault Zone. *Mineralogy and Petrology*, 114(5), 413-434.
 594 <https://doi.org/10.1007/s00710-020-00706-y>
 595 Robinson, A.C. (2009a). Geologic offsets across the northern Karakorum fault: Implications
 596 for its role and terrane correlations in the western Himalayan-Tibetan orogen. *Earth*

597 *and Planetary Science Letters*, 279(1-2), 123-130.

598 <https://doi.org/10.1016/j.epsl.2008.12.039>

599 Robinson, A.C. (2009b). Evidence against Quaternary slip on the northern Karakorum Fault
600 suggests kinematic reorganization at the western end of the Himalayan–Tibetan
601 orogen. *Earth and Planetary Science Letters*, 286(1-2), 158-170.

602 <https://doi.org/10.1016/j.epsl.2009.06.025>

603 Robinson, A.C., Owen, L.A., Chen, J., Schoenbohm, L.M., Hedrick, K.A., Blisniuk, K.,
604 Sharp, W.D., Imrecke, D.B., Li, W., Yuan, Z., & Caffee, M.W. (2015). No late
605 Quaternary strike-slip motion along the northern Karakoram fault. *Earth and*
606 *Planetary Science Letters*, 409, 290-298. <https://doi.org/10.1016/j.epsl.2014.11.011>

607 Rolland, Y., Mahéo, G., Pecher, A., & Villa, I.M. (2009). Syn-kinematic emplacement of the
608 Pangong metamorphic and magmatic complex along the Karakorum Fault (N
609 Ladakh). *Journal of Asian Earth Sciences*, 34(1), 10-25.

610 <https://doi.org/10.1016/j.jseaes.2008.03.009>

611 Rosenberg, C.L., & Stünitz, H. (2003). Deformation and recrystallization of plagioclase along
612 a temperature gradient: an example from the Bergell tonalite. *Journal of Structural*
613 *Geology*, 25(3), 389-408. [https://doi.org/10.1016/S0191-8141\(02\)00036-6](https://doi.org/10.1016/S0191-8141(02)00036-6)

614 Ross, J.V., & Wilks, K.R. (1996). Microstructure development in an experimentally sheared
615 orthopyroxene granulite. *Tectonophysics*, 256(1-4), 83-100.

616 [https://doi.org/10.1016/0040-1951\(95\)00168-9](https://doi.org/10.1016/0040-1951(95)00168-9)

617 Schmid, S.M., & Casey, M. (1986). Complete fabric analysis of some commonly observed
618 quartz c-axis patterns. *Geophysical Monograph*, 36(6), 263-286.

619 Schwab, M., Ratschbacher, L., Siebel, W., McWilliams, M., Minaev, V., Lutkov, V., Chen,
620 F., Stanek, K., Nelson, B., Frisch, W., & Wooden, J.L. (2004). Assembly of the
621 Pamirs: Age and origin of magmatic belts from the southern Tien Shan to the

southern Pamirs and their relation to Tibet. *Tectonics*, 23(4).

<https://doi.org/10.1029/2003TC001583>

Searle, M.P., & Phillips, R.J. (2007). Relationships between right-lateral shear along the Karakoram fault and metamorphism, magmatism, exhumation and uplift: evidence from the K2–Gasherbrum–Pangong ranges, north Pakistan and Ladakh. *Journal of the Geological Society*, 164(2), 439-450. <https://doi.org/10.1144/0016-76492006-072>

Searle, M.P., Weinberg, R.F., & Dunlap, W.J. (1998). Transpressional tectonics along the Karakoram fault zone, northern Ladakh: constraints on Tibetan extrusion. *Geological Society, London, Special Publications*, 135(1), 307-326.

<https://doi.org/10.1144/GSL.SP.1998.135.01.20>

Sen, K., Mukherjee, B.K., & Collins, A.S. (2014). Interplay of deformation and magmatism in the Pangong Transpression Zone, eastern Ladakh, India: Implications for remobilization of the trans-Himalayan magmatic arc and initiation of the Karakoram Fault. *Journal of Structural Geology*, 62, 13-24.

<https://doi.org/10.1016/j.jsg.2014.01.009>

Shimizu, I. (2008). Theories and applicability of grain size piezometers: The role of dynamic recrystallization mechanisms. *Journal of Structural Geology*, 30(7), 899-917.

<https://doi.org/10.1016/j.jsg.2008.03.004>

Stipp, M., & Tullis, J. (2003). The recrystallized grain size piezometer for quartz.

Geophysical Research Letters, 30(21). <https://doi.org/10.1029/2003GL018444>

Stipp, M., Stünitz, H., Heilbronner, R., & Schmid, S.M. (2002). Dynamic recrystallization of quartz: correlation between natural and experimental conditions. *Geological Society, London, Special Publications*, 200(1), 171-190.

<https://doi.org/10.1144/GSL.SP.2001.200.01.11>

646 Stipp, M., Tullis, J., Scherwath, M., & Behrmann, J.H. (2010). A new perspective on
 647 paleopiezometry: Dynamically recrystallized grain size distributions indicate
 648 mechanism changes. *Geology*, 38(8), 759-762. <https://doi.org/10.1130/G31162.1>
 649 Takahashi, M., Nagahama, H., Masuda, T., & Fujimura, A. (1998). Fractal analysis of
 650 experimentally, dynamically recrystallized quartz grains and its possible application
 651 as a strain rate meter. *Journal of structural Geology*, 20(2-3), 269-275.
 652 [https://doi.org/10.1016/S0191-8141\(97\)00072-2](https://doi.org/10.1016/S0191-8141(97)00072-2)
 653 Tamura, T., Oohashi, K., Otsubo, M., Miyakawa, A., & Niwa, M. (2020). Contribution to
 654 crustal strain accumulation of minor faults: a case study across the Niigata–Kobe
 655 Tectonic Zone, Japan. *Earth, Planets and Space*, 72 (7).
 656 <https://doi.org/10.1186/s40623-020-1132-5>
 657 Tapponnier, P., Peltzer, G.L.D.A.Y., Le Dain, A.Y., Armijo, R., & Cobbold, P. (1982).
 658 Propagating extrusion tectonics in Asia: New insights from simple experiments with
 659 plasticine. *Geology*, 10(12), 611-616.
 660 [https://doi.org/10.1130/0091-7613\(1982\)10<611:PETIAN>2.0.CO;2](https://doi.org/10.1130/0091-7613(1982)10<611:PETIAN>2.0.CO;2)
 661
 662 Tullis, J., Stünitz, H., Teyssier, C., & Heilbronner, R. (2000). Deformation microstructures in
 663 quartzo-feldspathic rocks. *Journal of the Virtual Explorer*, 2.
 664 [10.3809/jvirtex.2000.00019](https://doi.org/10.3809/jvirtex.2000.00019)
 665 Twiss, R.J. (1977). Theory and applicability of a recrystallized grain size paleopiezometer. In
 666 *Stress in the Earth* (227-244). Birkhäuser, Basel. 10.1007/978-3-0348-5745-1_13
 667 Twiss, R.J., & Moores, E.M. (1992). *Structural geology*. Macmillan.
 668 Valli, F., Leloup, P.H., Paquette, J.L., Arnaud, N., Li, H., Tapponnier, P., Lacassin, R.,
 669 Guillot, S., Liu, D., Deloule, E., & Xu, Z. (2008). New U-Th/Pb constraints on

- timing of shearing and long-term slip-rate on the Karakorum fault. *Tectonics*, 27(5).
<https://doi.org/10.1029/2007TC002184>
- Vernon, R.H. (2004). *A practical guide to rock microstructure*. Cambridge university press.
- Vigneresse, J.L., & Burg, J.P. (2004). Strain-rate-dependent rheology of partially molten rocks. *Geological Society, London, Special Publications*, 227(1), 327-336.
<https://doi.org/10.1144/GSL.SP.2004.227.01.17>
- Wallis, D., Carter, A., Phillips, R.J., Parsons, A.J., & Searle, M.P. (2016). Spatial variation in exhumation rates across Ladakh and the Karakoram: New apatite fission track data from the Eastern Karakoram, NW India. *Tectonics*, 35(3), 704-721.
<https://doi.org/10.1002/2015TC003943>
- Weinberg, R.F., Dunlap, W.J., & Whitehouse, M. (2000). New field, structural and geochronological data from the Shyok and Nubra valleys, northern Ladakh: linking Kohistan to Tibet. *Geological Society, London, Special Publications*, 170(1), 253-275. <https://doi.org/10.1144/GSL.SP.2000.170.01.14>
- Weinberg, R.F., Mark, G., & Reichardt, H. (2009). Magma ponding in the Karakoram shear zone, Ladakh, NW India. *Geological Society of America Bulletin*, 121(1-2), 278-285.
<https://doi.org/10.1130/B26358.1>

Figure captions

Figure 1 a) Map of the Karakoram terrane. Study area is represented by the red-coloured dashed box. Inset shows the Karakoram terrane on the map of India (adapted and modified after Pundir et al., 2020b). b) Geological map of the area showing the major lithologies, the planar and linear structural elements (adapted and modified after Pundir et al., 2020b). The Tangtse and the Muglib strands of the Karakoram Shear Zone (KSZ) are marked in orange colour. The present work is based primarily on locations TM 1 and TM 2 along the Tangtse

strand of the KSZ and the locations DS 6, DS 7 and DS 8 in the relatively less deformed part of the Tangtse Metamorphic Complex (TMC). Sample TM 2 is the key focus of this study.

Figure 2 Field photographs a) Granite gneiss and mylonitized amphibolite occurring in contact along the Tangtse strand of the KSZ. Note the concordance of the planar fabric (S) in the two lithologies. b) Dextrally sheared feldspathic domains in plan in the granite-gneisses along the KSZ. c) Sub-horizontal stretching lineation (L) on the steeply dipping mylonitic foliation surface in the granite gneisses along the KSZ. d) Sub-horizontal stretching lineation on the steeply dipping mylonitic foliation (S) in the mylonitized amphibolites.

Figure 3 Photomicrographs: a) Foliation in the granite gneisses, defined by alternate monomineralic layers of feldspar and quartz. Note the segregation between the feldspathic and the quartz-rich layers. b) Amoeboid sutures along the boundaries of quartz with the quartz ribbons. Note the deformation bands within some of the quartz grains. c) Core-mantle structure in feldspar. Note the sharp boundary between the core and the mantle of recrystallized grains. d) amphibole, biotite, feldspar and quartz in the deformed amphibolites of the Tangtse Metamorphic Complex (TMC). Note the preferred alignment of biotites and the lack of any alignment of the amphiboles. e) Foliation defined by a preferred orientation of biotites and quartz ribbon in the deformed amphibolites. Note the high wavelength sutures along the grain boundaries of quartz. f) Preferred orientation of biotites and deformed lamellar twining in plagioclase in the deformed amphibolites of the TMC. d) Core-mantle structures in the feldspathic domains of the granite gneisses. Note the sharp distinct boundaries between the core and the mantle of recrystallized grains.

Figure 4 Photomicrographs along the Tangtse strand of the KSZ: a, b) Coarse-grained monomineralic quartz-rich layers (CGQL) alternating with amphibole-biotite-quartz rich polymineralic layers (AMBIORL). Note the considerably finer grain size of quartz in the

AMBIORL as compared to the quartz in the CGQL. c, d) Consistent association of the finer-grained quartz with the amphibole-biotite bearing domains in the AMBIORL. Note the increase in grain-size of quartz with distance from the amphiboles and biotites. Points P and P' have been used to calculate displacement accommodated by the CGQL due to shearing along the KSZ. Points Q and Q' have been utilized to determine displacement accommodated by the AMBIORL during shearing. e) Microstructure of quartz in the CGQL. Note the amoeboid grain boundaries in all directions with respect to the individual quartz grains as well as the high-wavelength sutures along the grain-boundaries f) Microstructures of quartz in both the CGQL and the AMBIORL. Note that both in the CGQL and the AMBIORL quartz grains show high wavelength sutures along amoeboid grain boundaries. Also note that pinning of quartz by amphiboles and biotites restricts GBM in quartz at high angles to the foliation in the AMBIORL.

Figure 5 Diagram (adapted from and modified after Law, 2014) showing the ranges of strain-rate at which GBM (Green dashed lines) and BLG (Yellow dashed lines) can operate in the quartz grains deformed along the KSZ at 550-600 °C Yellow lines. Note that for BLG operates at strain rates, at least 10^2 to 10^5 times higher than that required for GBM at 550-600 °C. Orange dashed line represents the strain-rate values calculated along the KSZ by Boutonnet et al. (2013).

Figure 6 Schematic diagram showing the stages of evolution of the amphibolites during deformation along the KSZ. a) distribution of amphiboles, biotites and quartz in the relatively low strain domains (in the TMC) with respect to the KSZ b) Increase in strain along the mylonitic strands of the KSZ resulted in the segregation of the amphiboles and biotites into layers (AMBIORL) alternating with monomineralic quartz-rich layers (CGQL). Modal proportion of quartz in Circular area, A in the AMBIORL is lower than the modal proportion of quartz in identical circular area, A in the CGQL. c) Greater nucleation of dynamically

recrystallized grains in the AMBIORL owing to a greater accommodation of strain by the quartz at higher strain-rate per unit area, adjacent to the amphiboles and biotites (that did not accommodate significant strain) than the quartz in the CGQL, away from the amphiboles and biotites.

Figure 7 Diagram showing the variations in displacement from the micro to regional scale if strain rate is partitioned in a proportion similar to that between the CGQL and the AMBIORL in mylonitized amphibolites of the KSZ. a) Displacement accommodated by the CGQL and the AMBIORL in microscopic scale. Note that the AMBIORL accommodates displacement (d') almost 2-3 km greater than the displacement accommodated by the CGQL (d). b) Assuming similar proportion of partitioning of strain rate between hypothetical layer 1 and hypothetical layer 2 in outcrop scale, layer 2 accommodates 850-1500 m greater than that accommodated by layer 1. c) Assuming similar proportion of partitioning of strain rate between hypothetical layer 1 and hypothetical layer 2 in regional scale, layer 2 accommodates 100-200 km greater than that accommodated by layer 1.

Table 1 Table showing the values of the mean grain size (D) for the CGQL and the AMBIORL, respectively, calculated using the formulations of Christie and Ord (1980).

Appendix

Estimated displacements accommodated by the CGQL and the AMBIORL assuming that the CGQL deformed at a rate of $1.6 \times 10^{-13} \text{ s}^{-1}$ from 27-15 Ma (timing of shearing along the KSZ). Similar calculations, extrapolated to hypothetical layers 1 and 2 to have an estimate of the displacements accommodated in outcrop scale (10 m: assumed thickness of each layer) and regional scale (1.25 km: assumed thickness of each layer) under conditions of similar proportion of strain-rate partitioning, as derived in equations 13-15, between layer 1 and layer

768 Displacement accommodated by CGQL and AMBIORL (micro-scale)

769 If, it is assumed that quartz in the CGQL deformed at a rate of $1.6 \times 10^{-13} \text{ s}^{-1}$ (Boutonnet et
770 al., 2013) then the quartz grains in the AMBIORL must have deformed at a rate in between

771 $2.34(1.6 \times 10^{-13}) \text{ s}^{-1}$ to $3.43(1.6 \times 10^{-13}) \text{ s}^{-1}$

772 as, $\dot{\epsilon}_{\text{AMBIORL}}/\dot{\epsilon}_{\text{CGQL}} = 2.34$ to 3.43 as per equations (13) to (15)

773 Therefore, quartz the AMBIORL deformed at a rate of $2.34 \times (1.6 \times 10^{-13}) \text{ s}^{-1}$ to $3.43 \times$
774 $(1.6 \times 10^{-13}) \text{ s}^{-1}$

775 Considering that deformation in the CGQL and the AMBIORL operated at these rates from
776 27-15 Ma (Pundir et al., 2020b) i.e., for a duration of 12 Ma, strain accommodated by the two
777 layers are:

778 $(\text{Strain})_{\text{CGQL}} = \dot{\epsilon}_{\text{CGQL}} \times (12 \times 10^6 \times 365 \times 24 \times 60 \times 60)$

779 $= 1.6 \times 10^{-13} \times 12 \times 10^6 \times 365 \times 24 \times 60 \times 60$

780 $= 1.6 \times 12 \times 365 \times 24 \times 36 \times 10^{-13} \times 10^6 \times 10^2$

781 $= 6054912 \times 10^{-5}$

782 $= 60.5$

783 $(\text{Strain})_{\text{AMBIORL}} = \dot{\epsilon}_{\text{CGQL}} \times (12 \times 10^6 \times 365 \times 24 \times 60 \times 60)$

784 $= 2.34 \times (1.6 \times 10^{-13} \times 12 \times 10^6 \times 365 \times 24 \times 60 \times 60)$ to $3.43 \times (1.6 \times 10^{-13} \times 12 \times 10^6 \times$
785 $365 \times 24 \times 60 \times 60)$

786 $= (2.34 \times 60.5)$ to (3.43×60.5)

787 $= 141.57$ to 207.5

788 Applying equation 2,

$$\begin{aligned}
& \text{Displacement (d) accommodated by CGQL} = (\text{Strain})_{\text{CGQL}} \times \text{width of CGQL} \\
& = 60.5 \times w; w: \text{width of CGQL (Fig. 4d)} \\
& = 60.5 \times 152.3 \mu\text{m} \\
& = 9214.15 \mu\text{m} \\
& = 0.92 \text{ cm (Fig. 7a)}
\end{aligned}$$

$$\begin{aligned}
& \text{Similarly, displacement (d') accommodated by AMBIORL} \\
& = (\text{Strain})_{\text{CGQL}} \times \text{width of AMBIORL} \\
& = (141.57 \text{ to } 207.5) \times w'; w': \text{width of AMBIORL (Fig. 4d)} \\
& = (141.57 \text{ to } 207.5) \times 197.1 \mu\text{m} \\
& = 27903.447 \mu\text{m to } 40898.35 \mu\text{m} = 2.79 \text{ cm to } 4.1 \text{ cm (Fig. 7a)}
\end{aligned}$$

Displacement accommodated by hypothetical layers 1 and 2 (outcrop scale)

If similar proportion of strain-rate partitioning are extrapolated to two hypothetical layers 1 and 2 (each 10 m thick) (Fig. 7b) such that layer 2 deforms at a rate 2.34 to 3.43 times that of layer 1 (Fig. 7b) and layer 1 deforms at $1.6 \times 10^{-13} \text{ s}^{-1}$ (Bouttonnet et al., 2013) then by similar calculations, over 12 Ma

$$\begin{aligned}
& \text{Displacement (d) accommodated by hypothetical layer 1} = 60.5 \times 10 \text{ m} = 605 \text{ m (Fig. 7b)} \\
& \text{and, Displacement (d) accommodated by hypothetical layer 1} = (141.57 \text{ to } 207.5) \times 10 \text{ m} \\
& = 1416 \text{ to } 2075 \text{ m (Fig. 7b)}
\end{aligned}$$

809 Displacement accommodated by hypothetical layers 1 and 2 (regional scale):

810 If similar proportion of strain-rate partitioning are extrapolated to two hypothetical layers 1
811 and 2 (each 1.25 km thick) (Fig. 7c) such that layer 2 deforms at a rate 2.34 to 3.43 times that
812 of layer 1 (Fig. 7c) and layer 1 deforms at $1.6 \times 10^{-13} \text{ s}^{-1}$ (Boutonnet et al., 2013) then by
813 similar calculations, over 12 Ma

814 Displacement (d) accommodated by hypothetical layer 1 = $60.5 \times 1.25 \text{ km} = 75.625 \text{ km}$ (Fig.
815 7c)

816 and, Displacement (d) accommodated by hypothetical layer 1 = $(141.57 \text{ to } 207.5) \times 1.25 \text{ km}$
817 $= 177 \text{ to } 259.37 \text{ km}$ (Fig. 7c)

818

819 Thus, in micro scale AMBIORL accommodates a displacement, 1.87-3.18 cm greater than
820 the CGQL. When strain-rate is partitioned in a proportion equal to $\dot{\epsilon}_{AMBIORL}/\dot{\epsilon}_{CGQL}$, between
821 hypothetical layers 1 and 2, layer 2 accommodates displacement 811-1470 m and 101-183
822 km greater than layer 1 in outcrop scale and regional scale, respectively.

823

824

LAYER IN MYLONITIZED AMPHIBOLITE (TM 2)	MEAN GRAIN SIZE (D; calculated after Christie and Ord, 1980)
Coarse grained quartz rich layer (CGQL)	127.5796 μm
Amphibole-biotite rich layer (AMBIORL)	57.83167 μm

Figure 1.

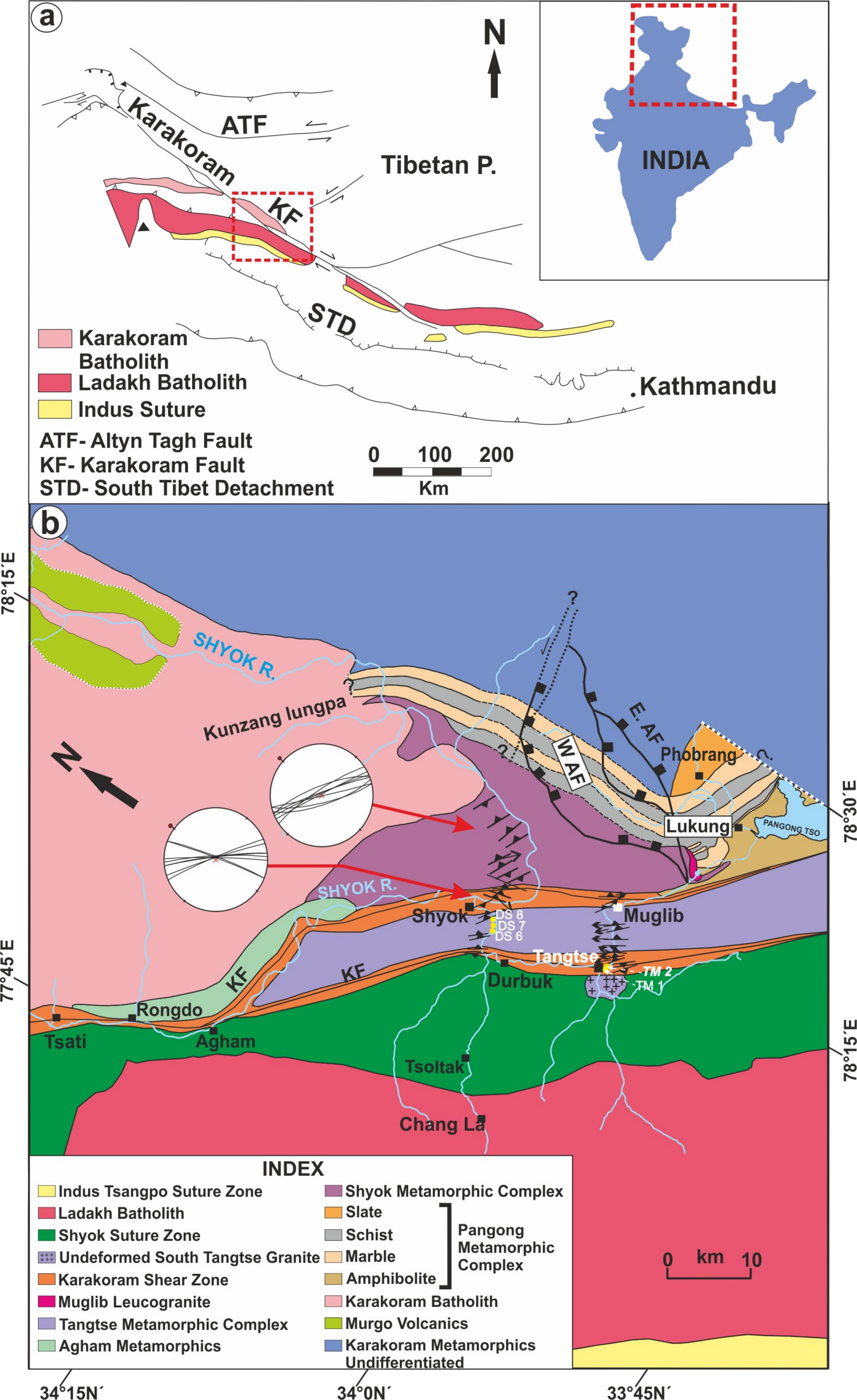


Figure 2.



Figure 3.

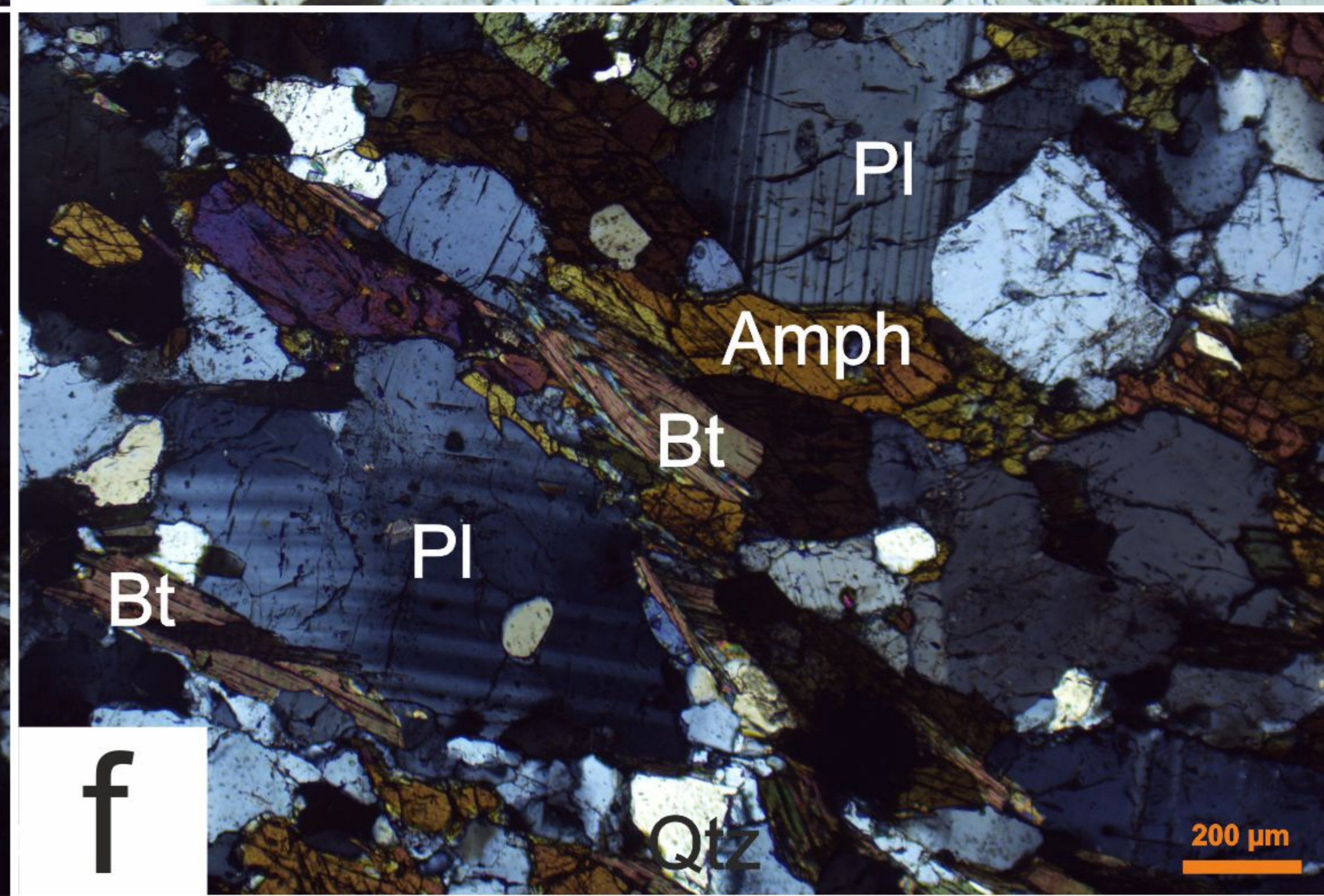
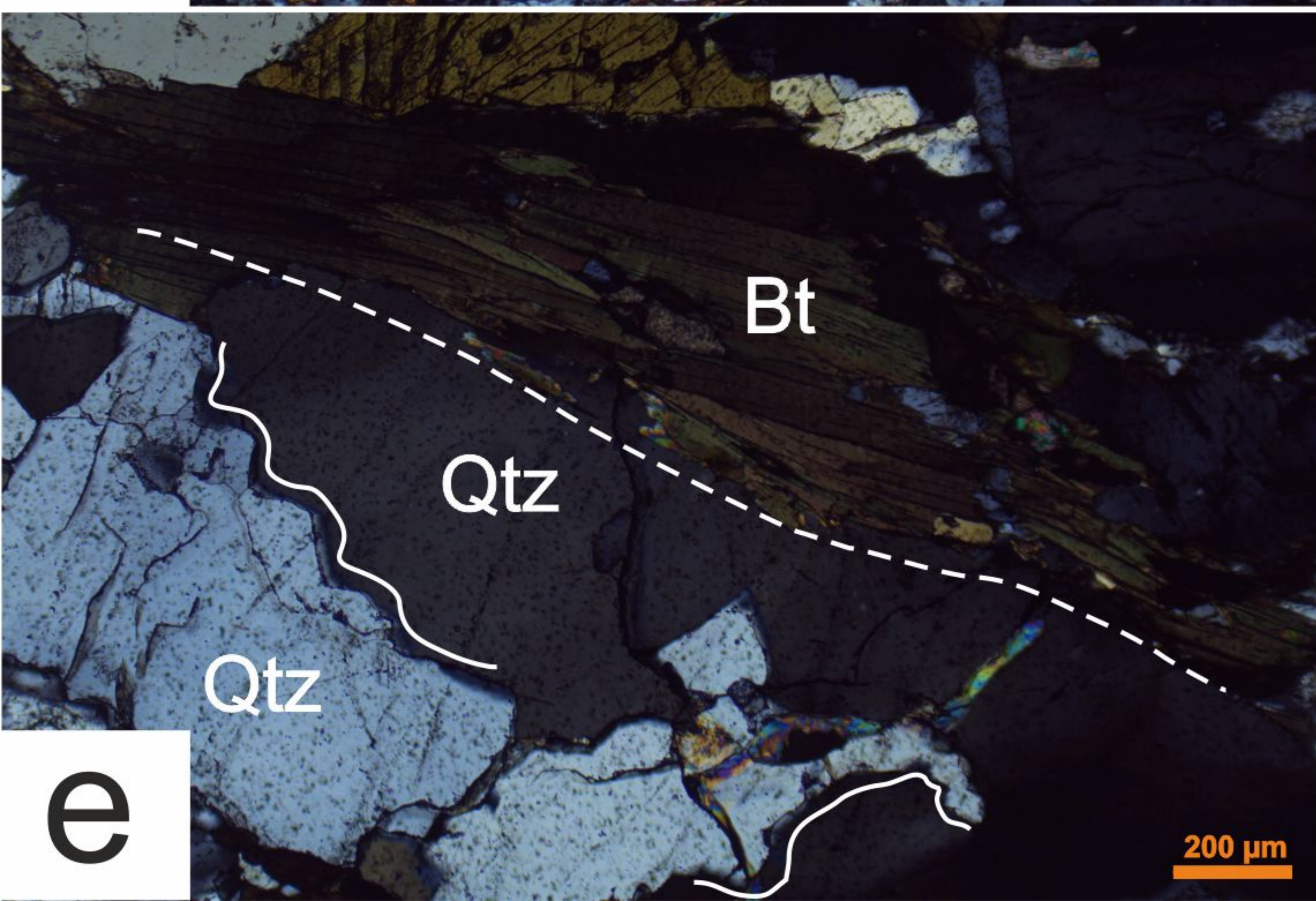
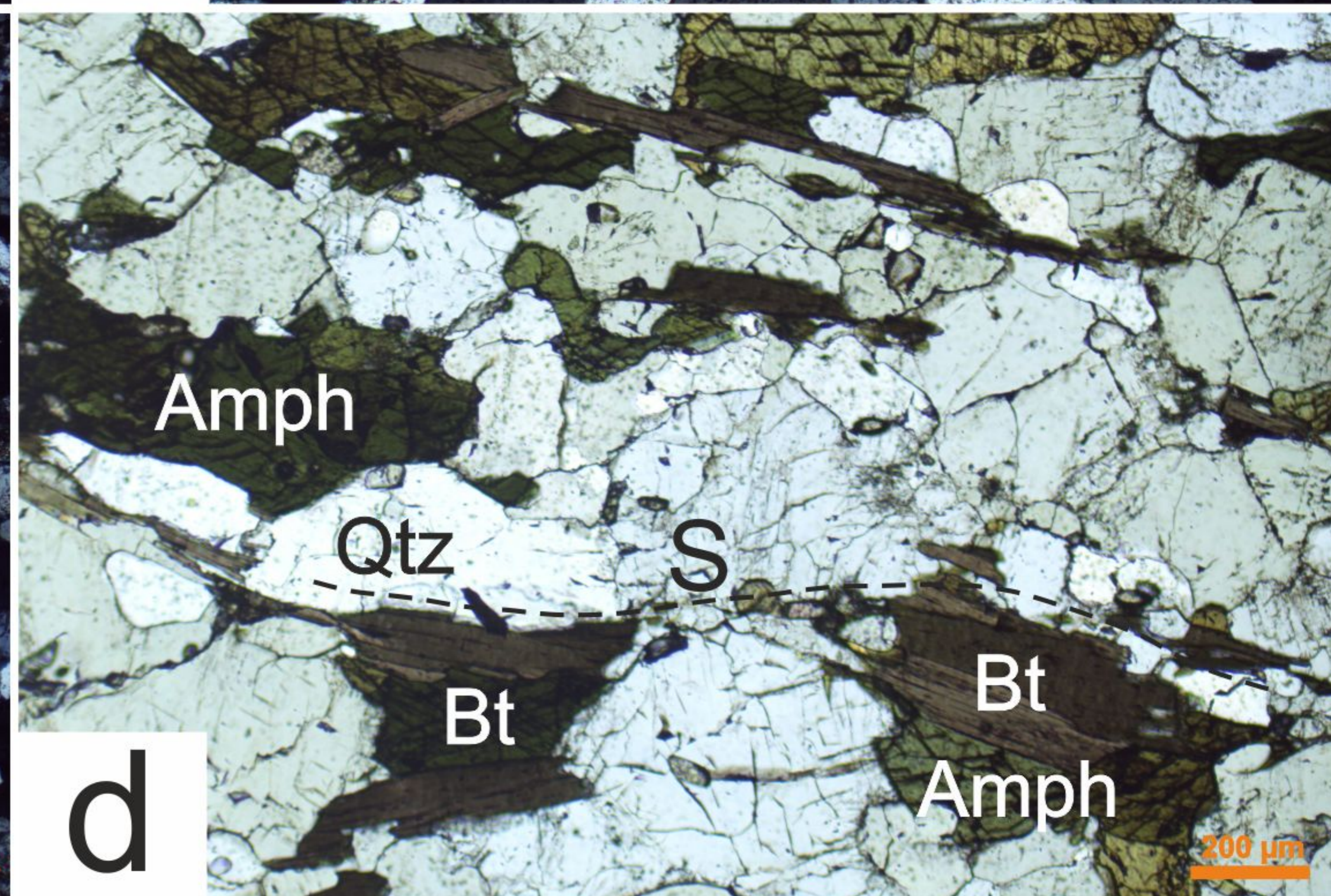
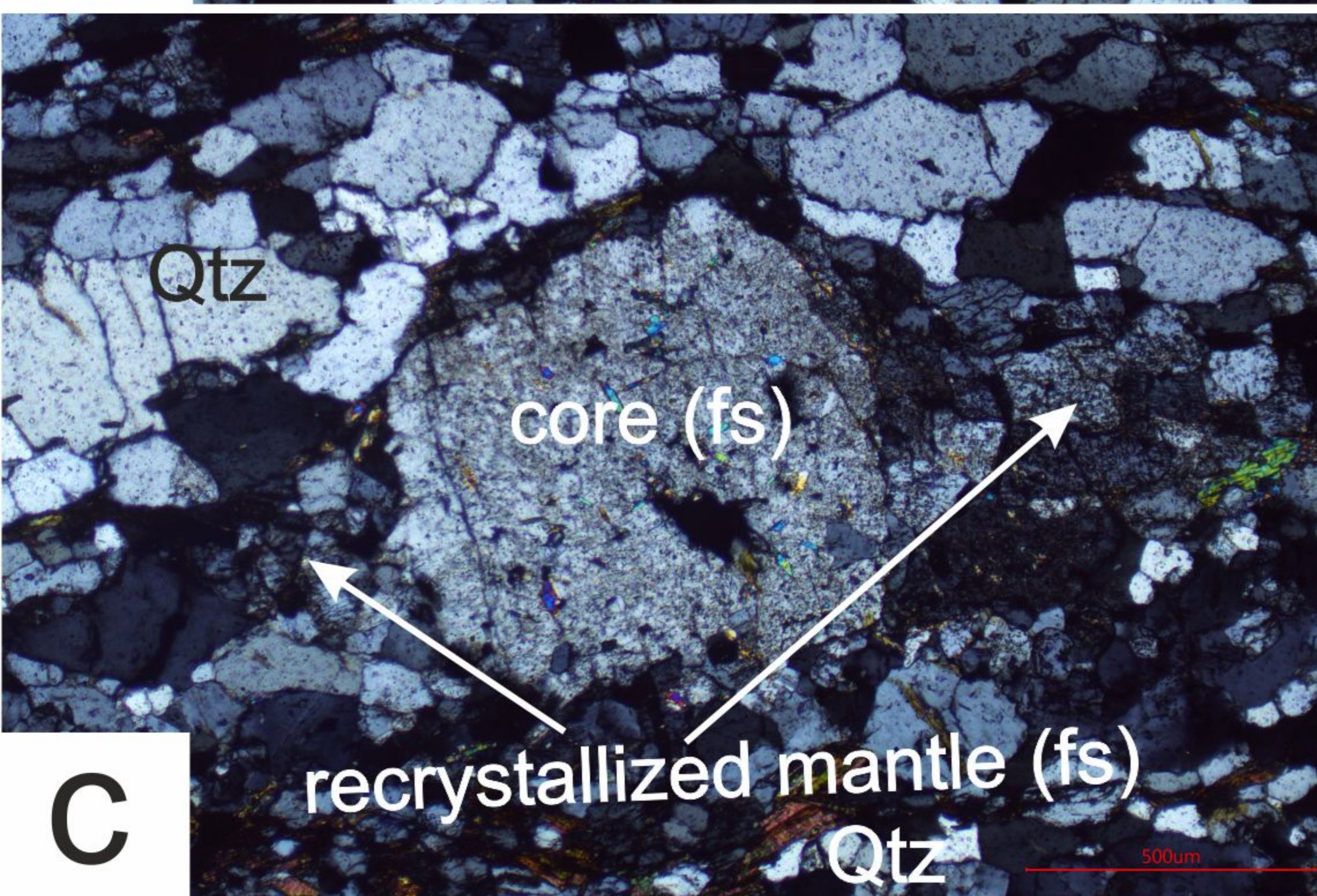
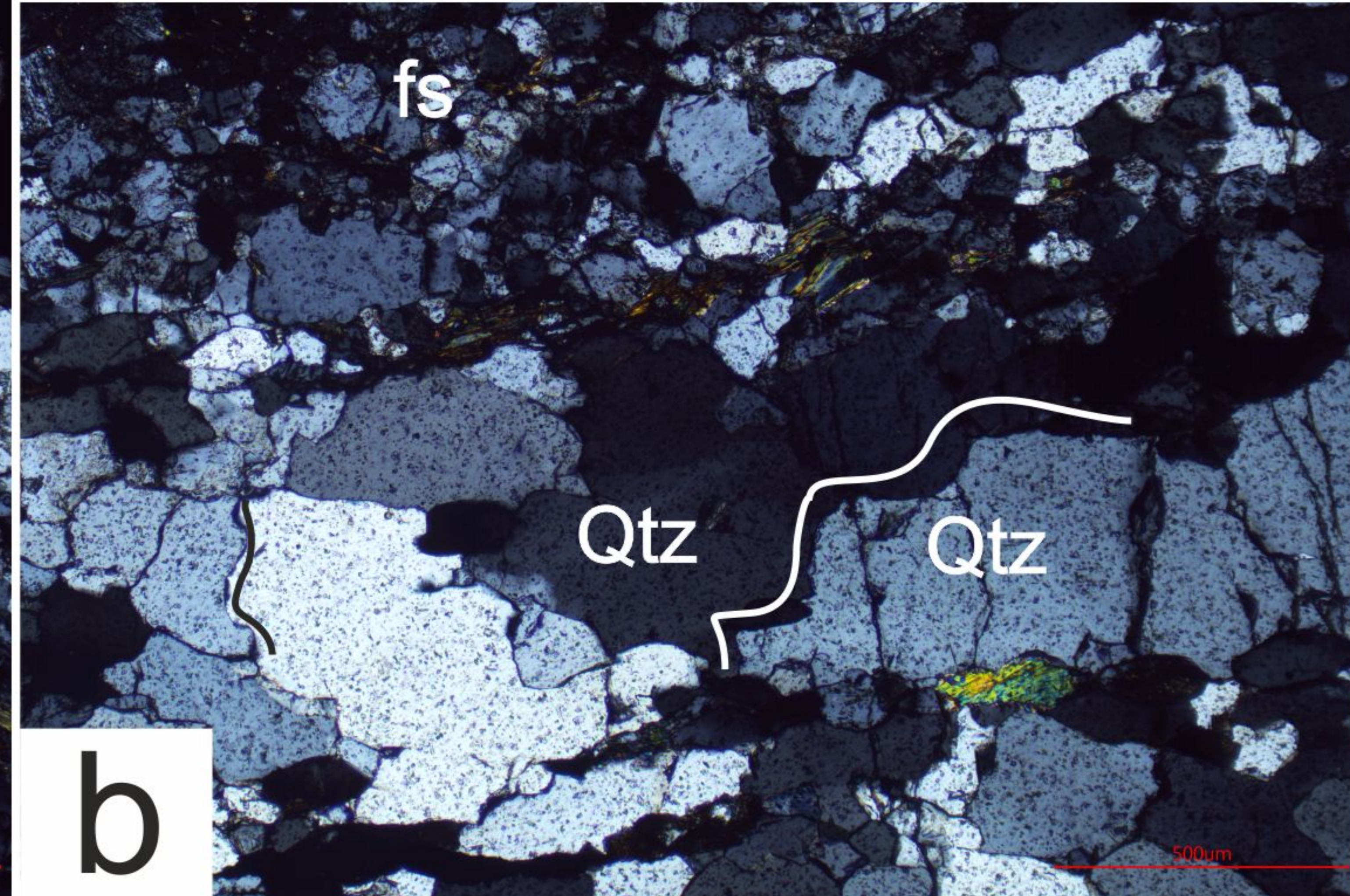
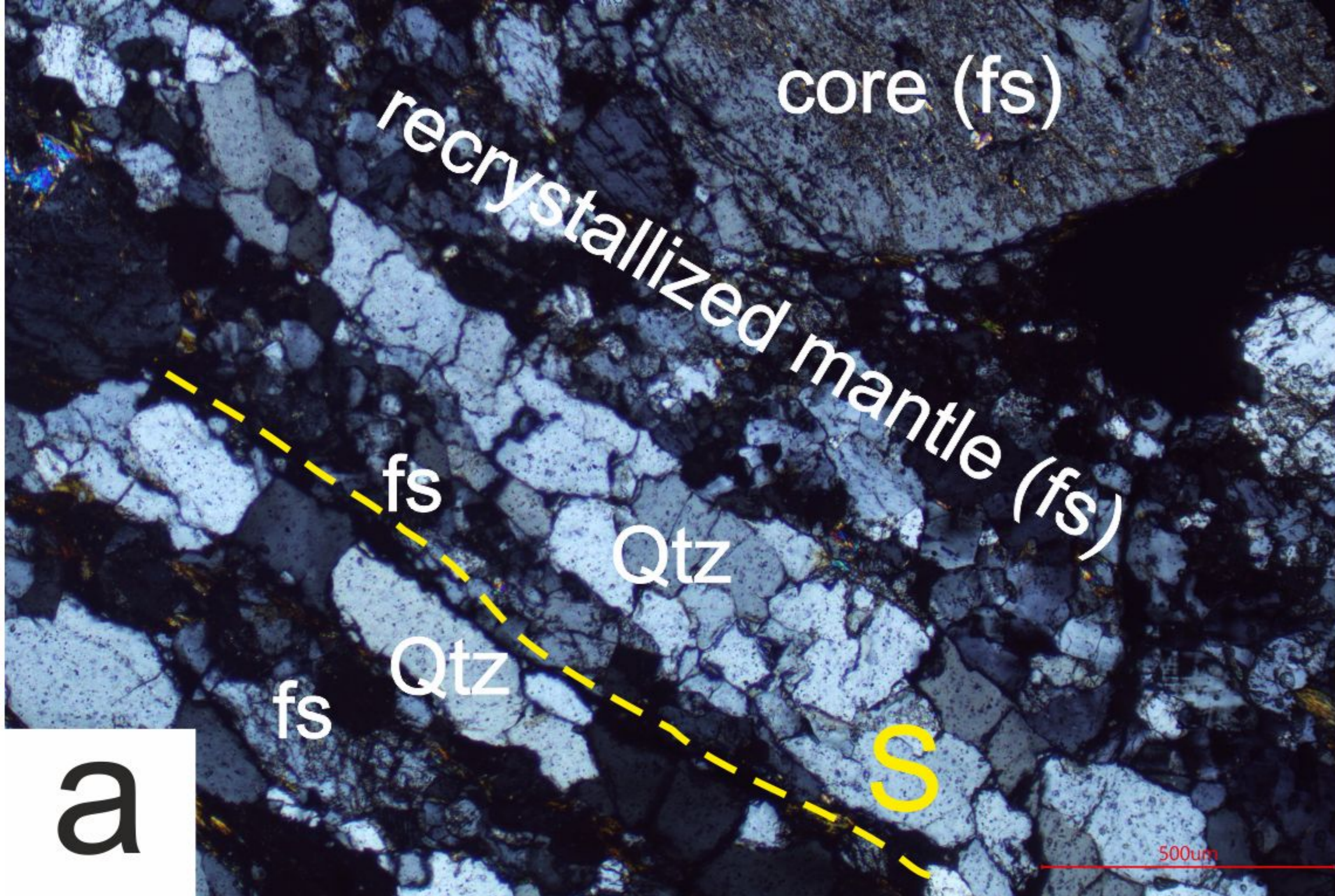


Figure 4.

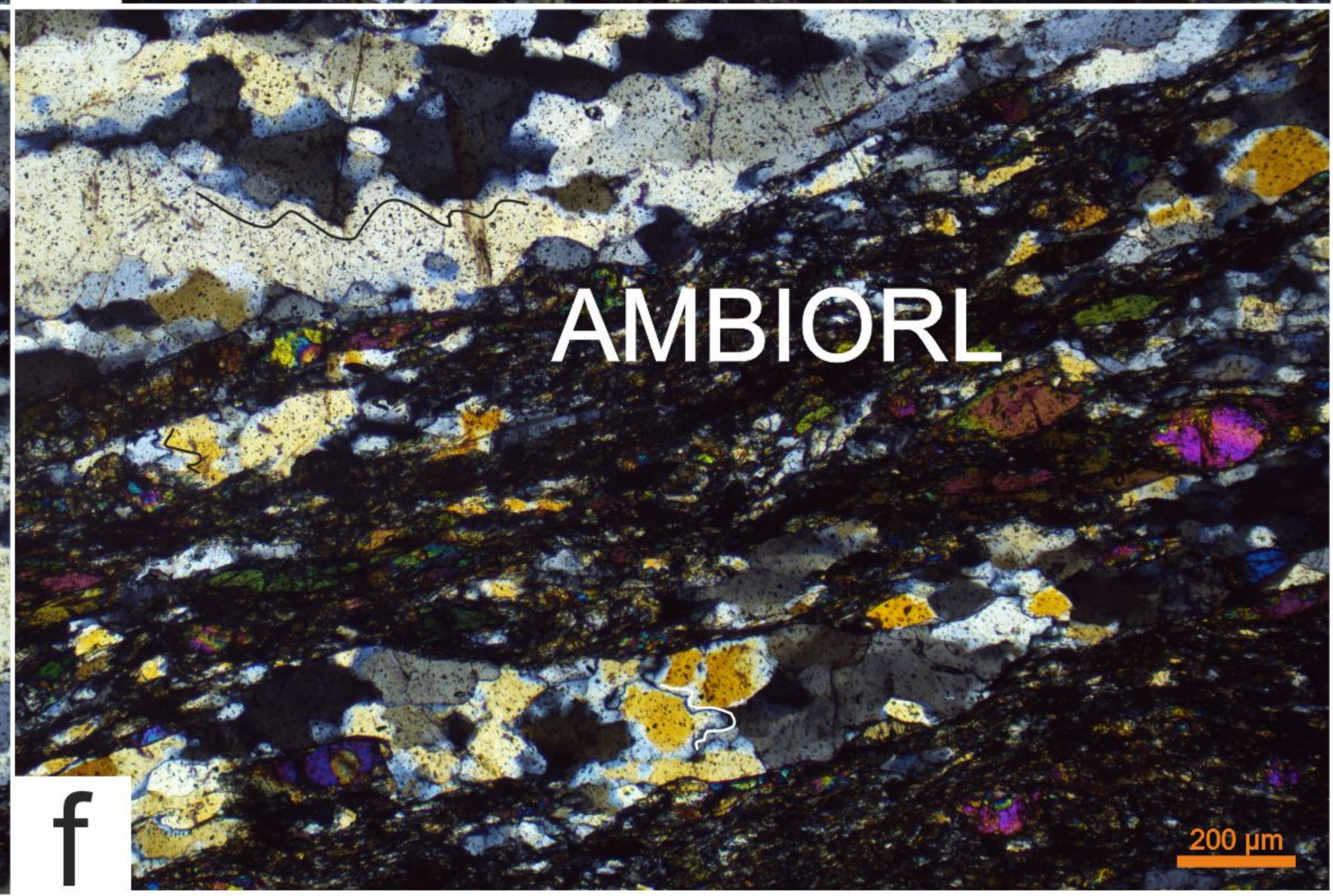
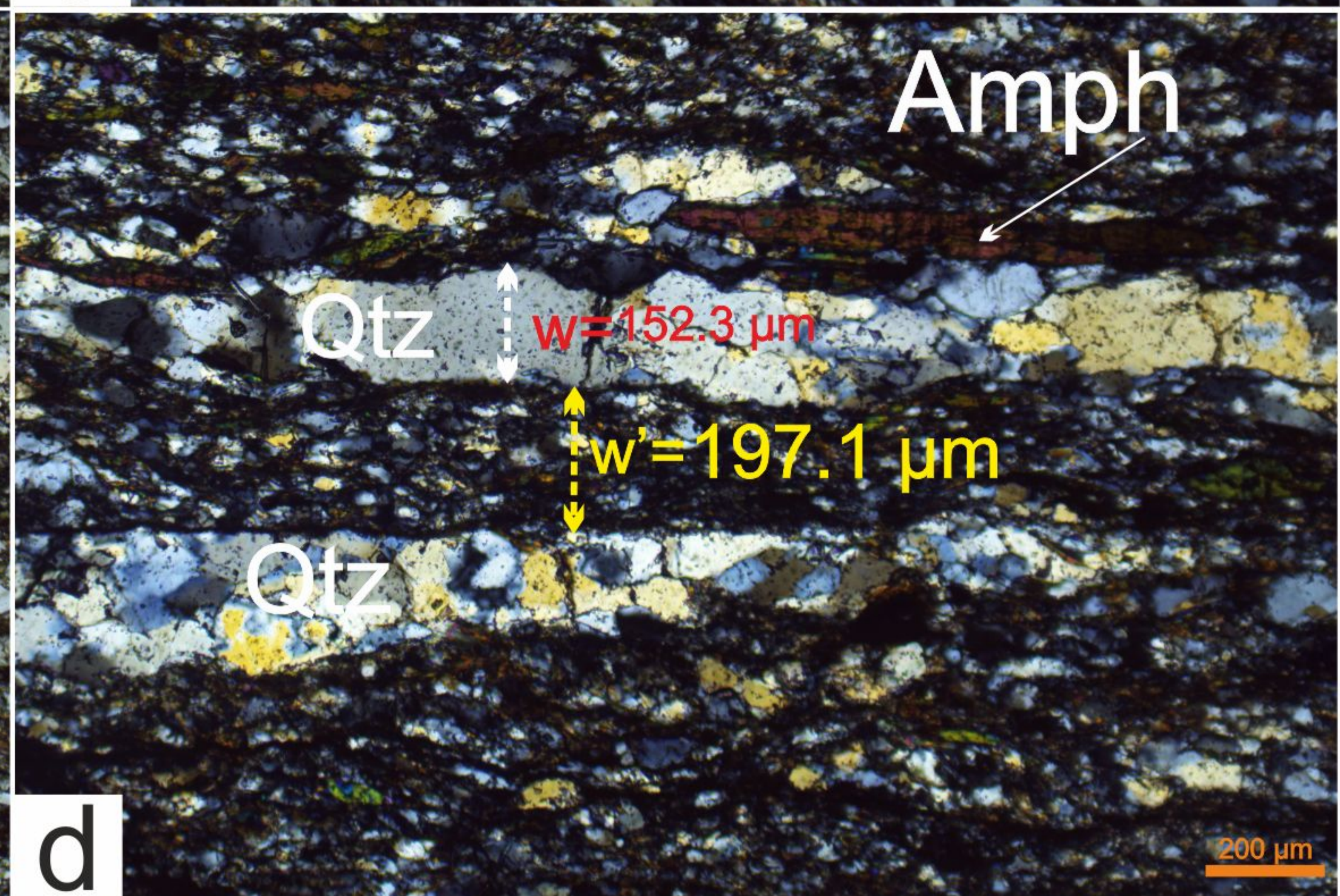
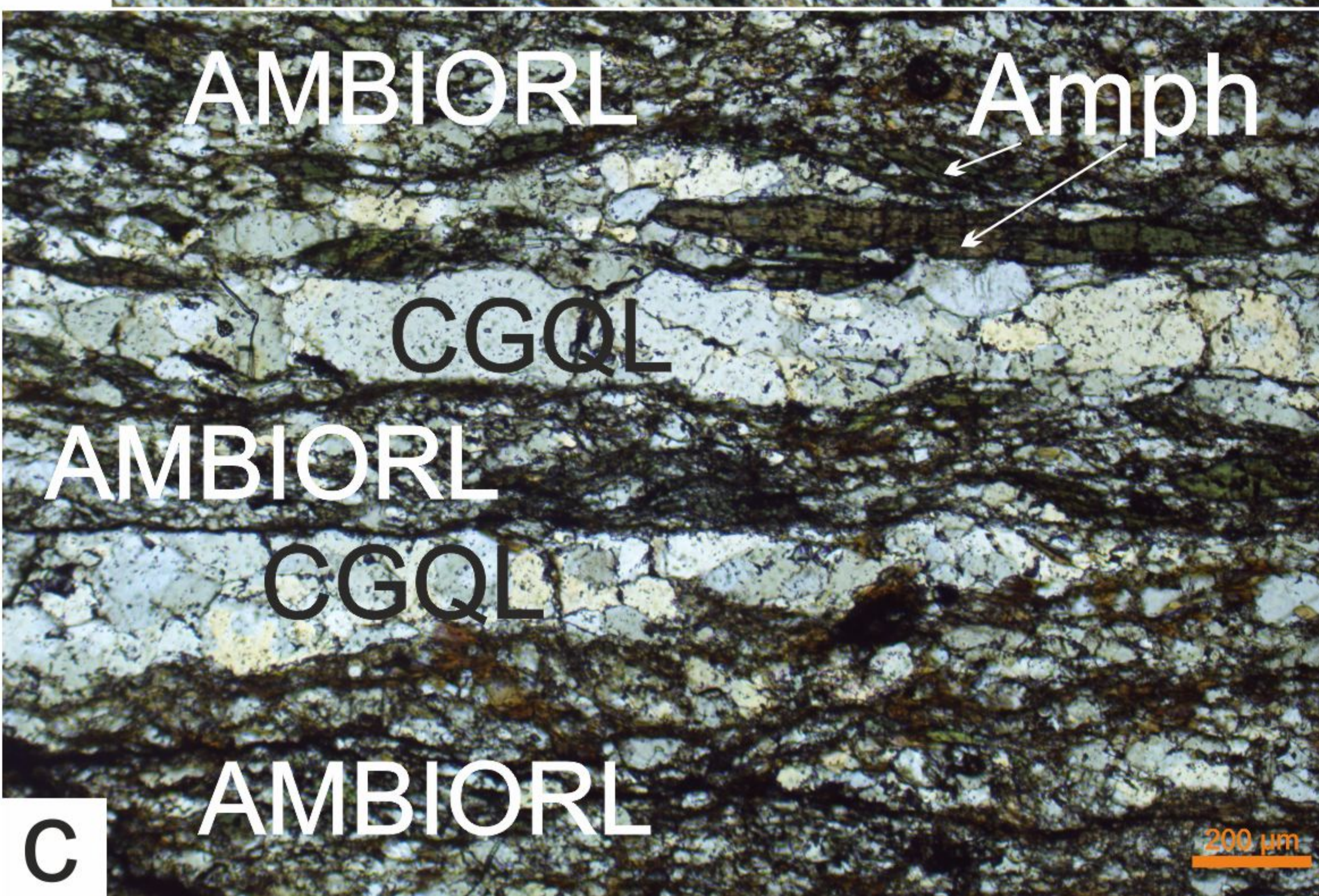
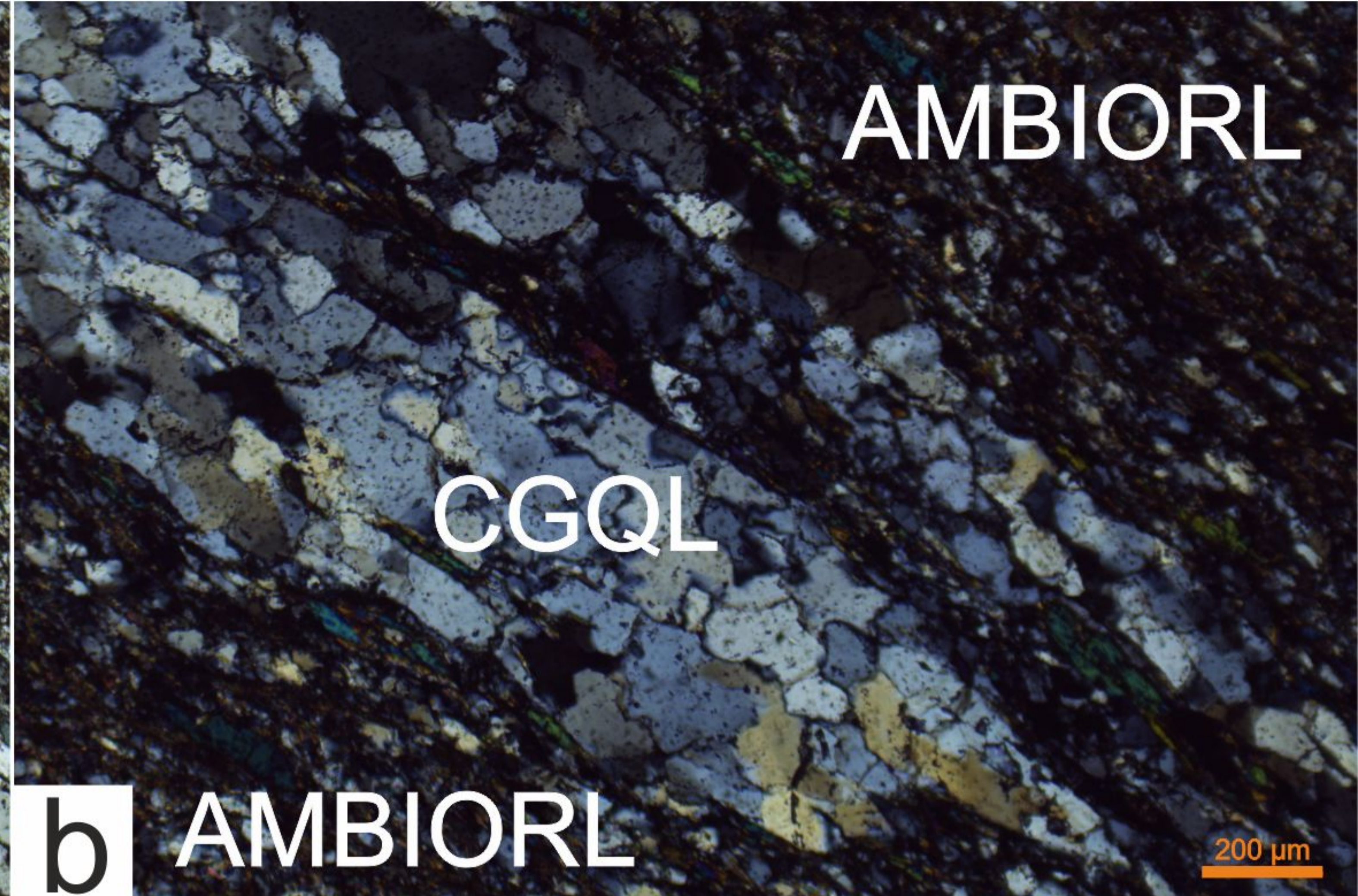
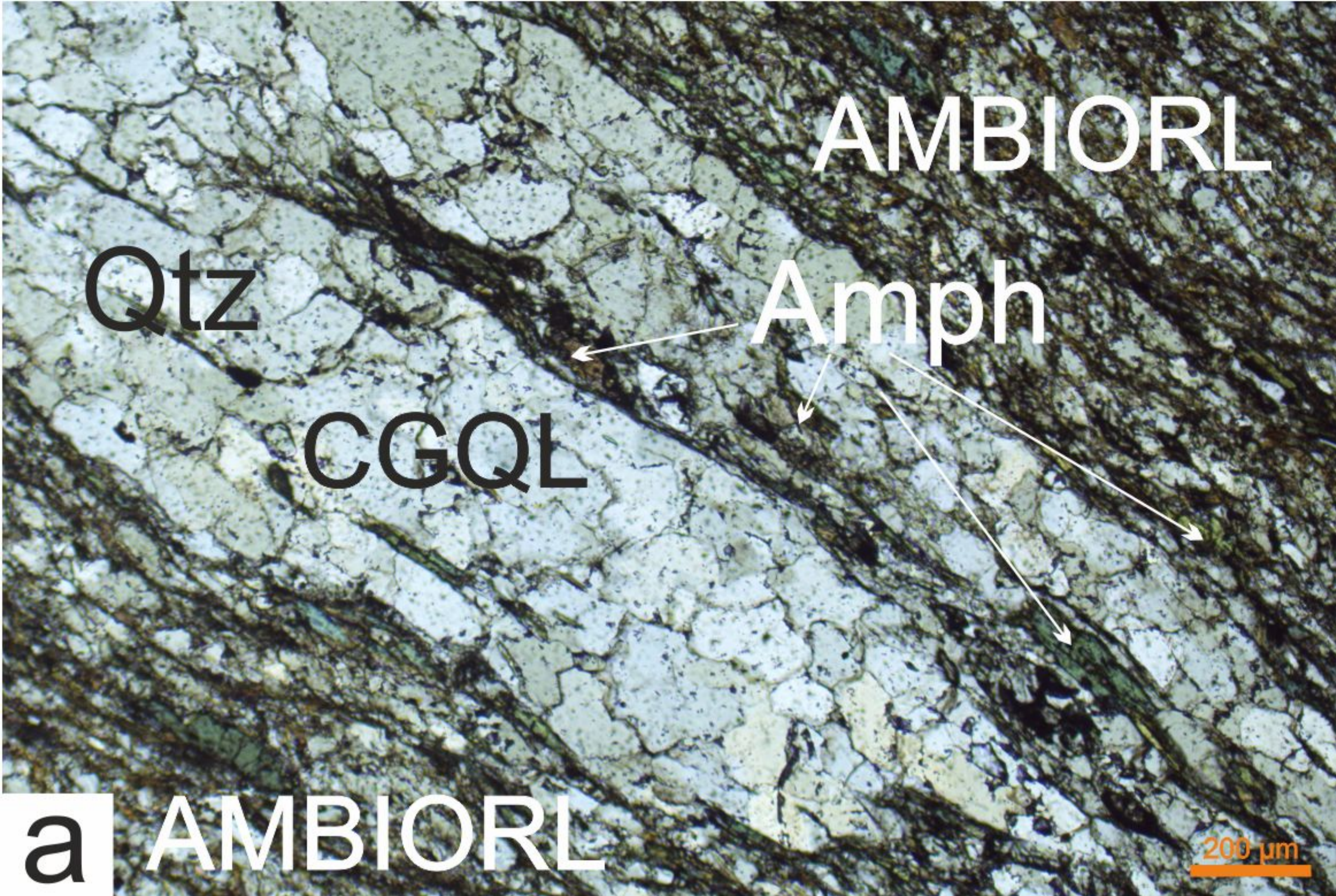
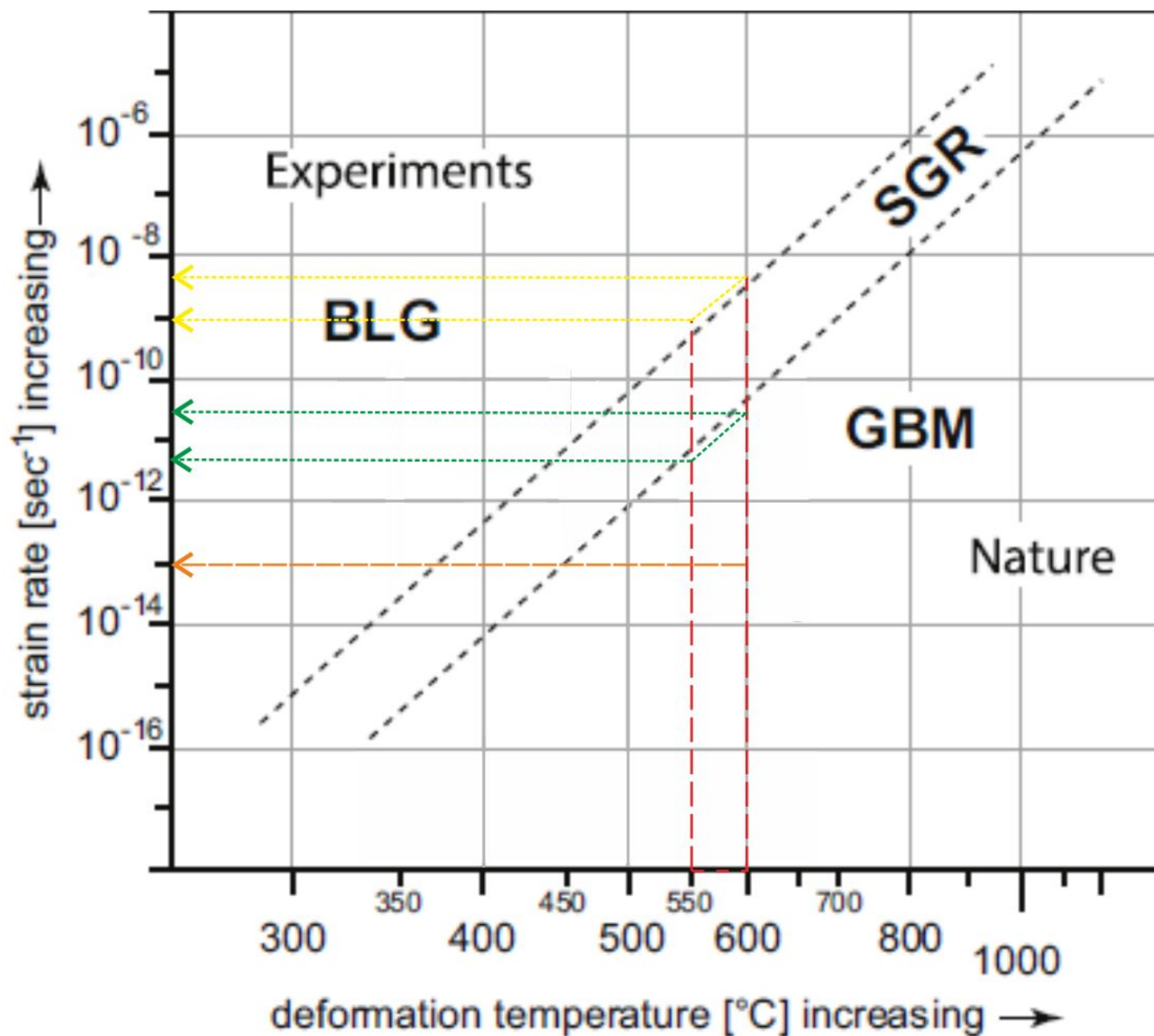


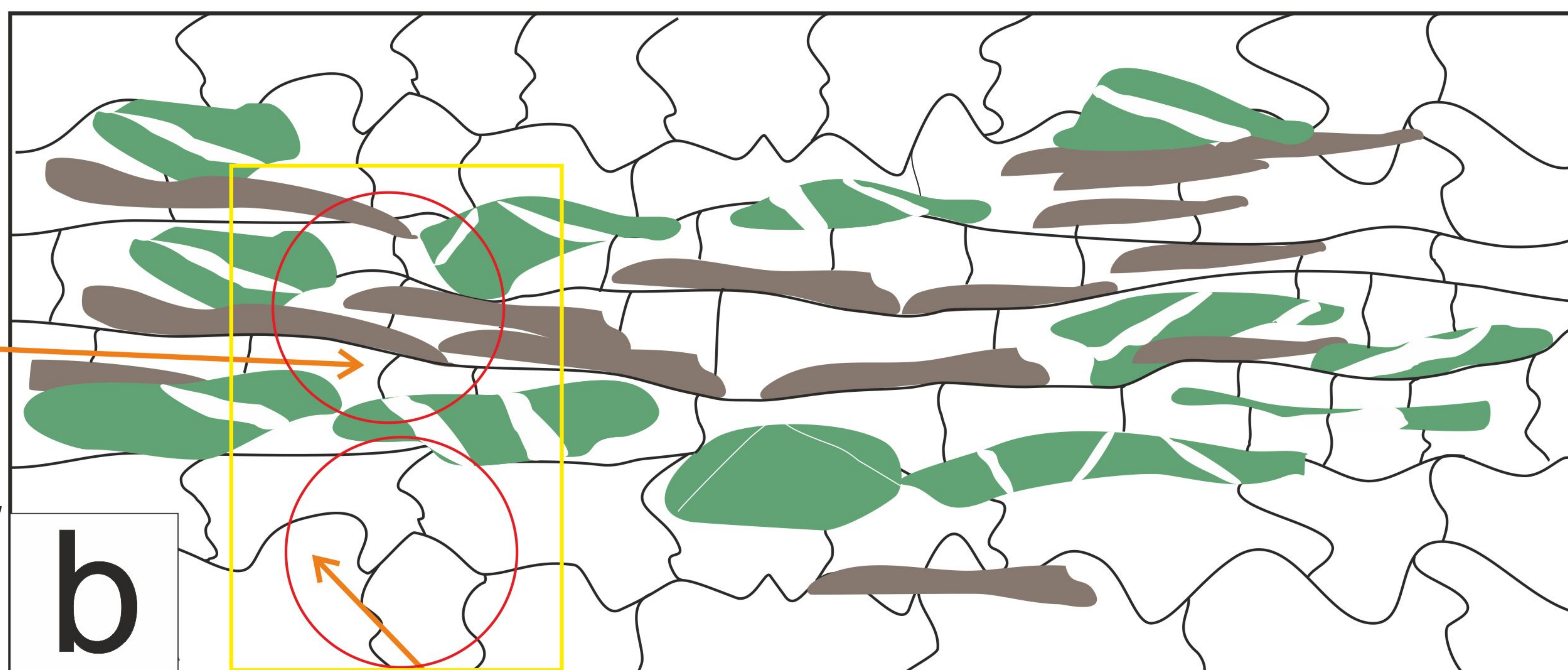
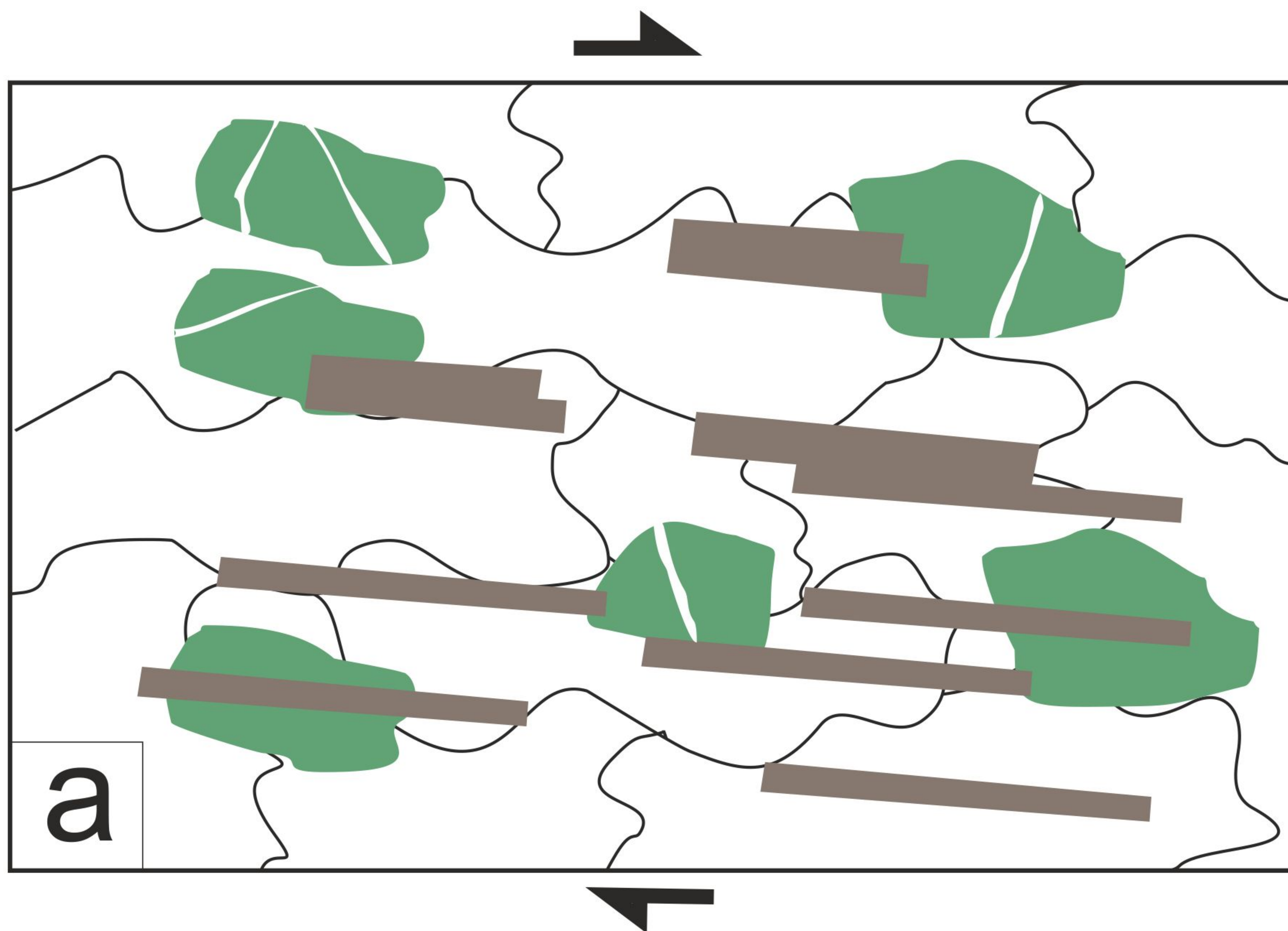
Figure 5.



- estimated strain-rates for BLG in quartz at 550-600 degree C
- estimated strain-rates for GBM in quartz at 550-600 degree C
- calculated strain-rate of quartz along the mylonitic strands of the KSZ (Bouttonnet et al., 2013)

Figure 6.

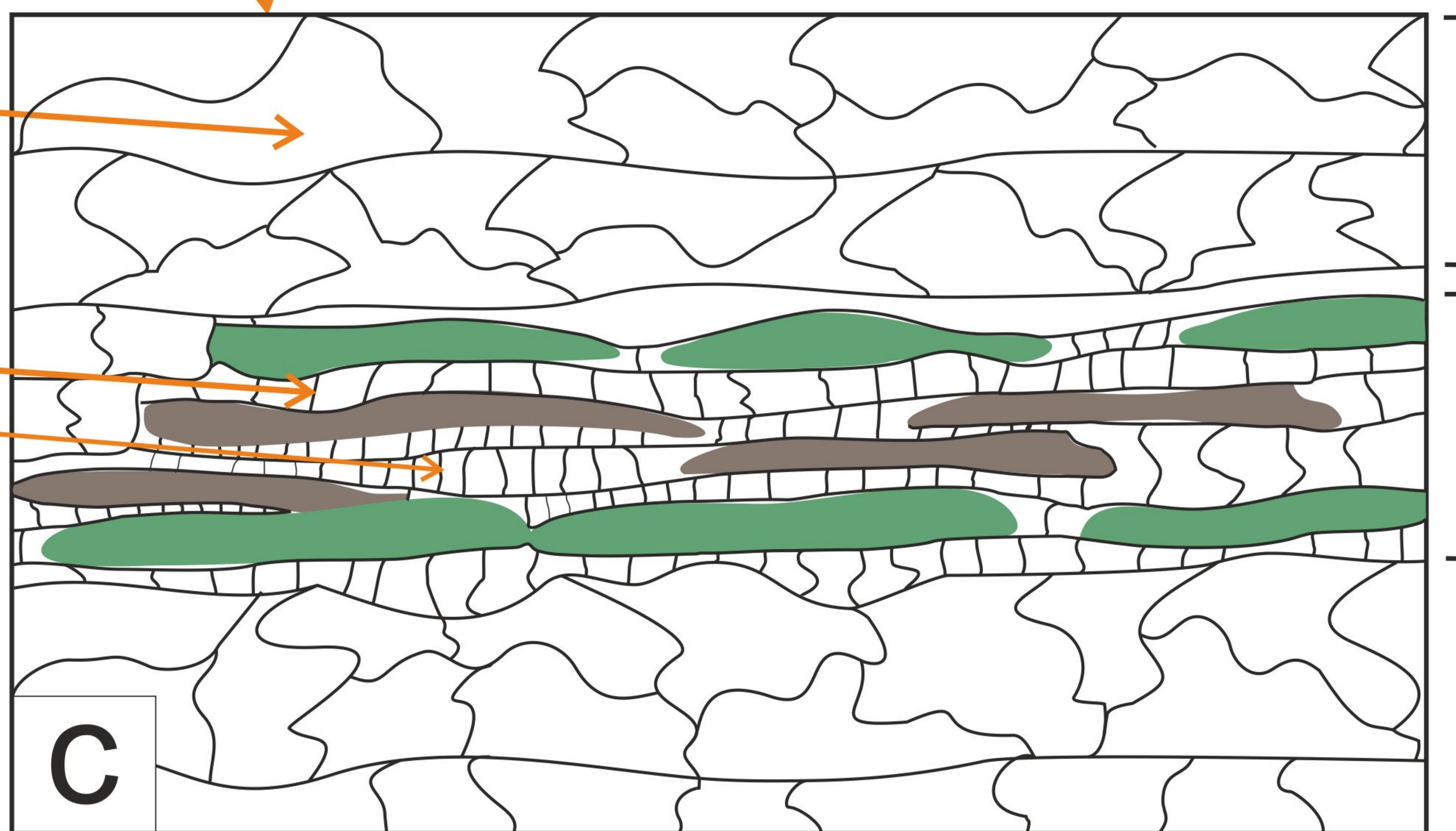
Low strain



*lower strain per
unit area of quartz
in monomineralic
quartz-rich layers*

*lower strain rate
per unit area
of quartz in the
CGQL*

*higher strain rate
per unit area
of quartz in the
AMBIORL*



CGQL

AMBIORL

High strain

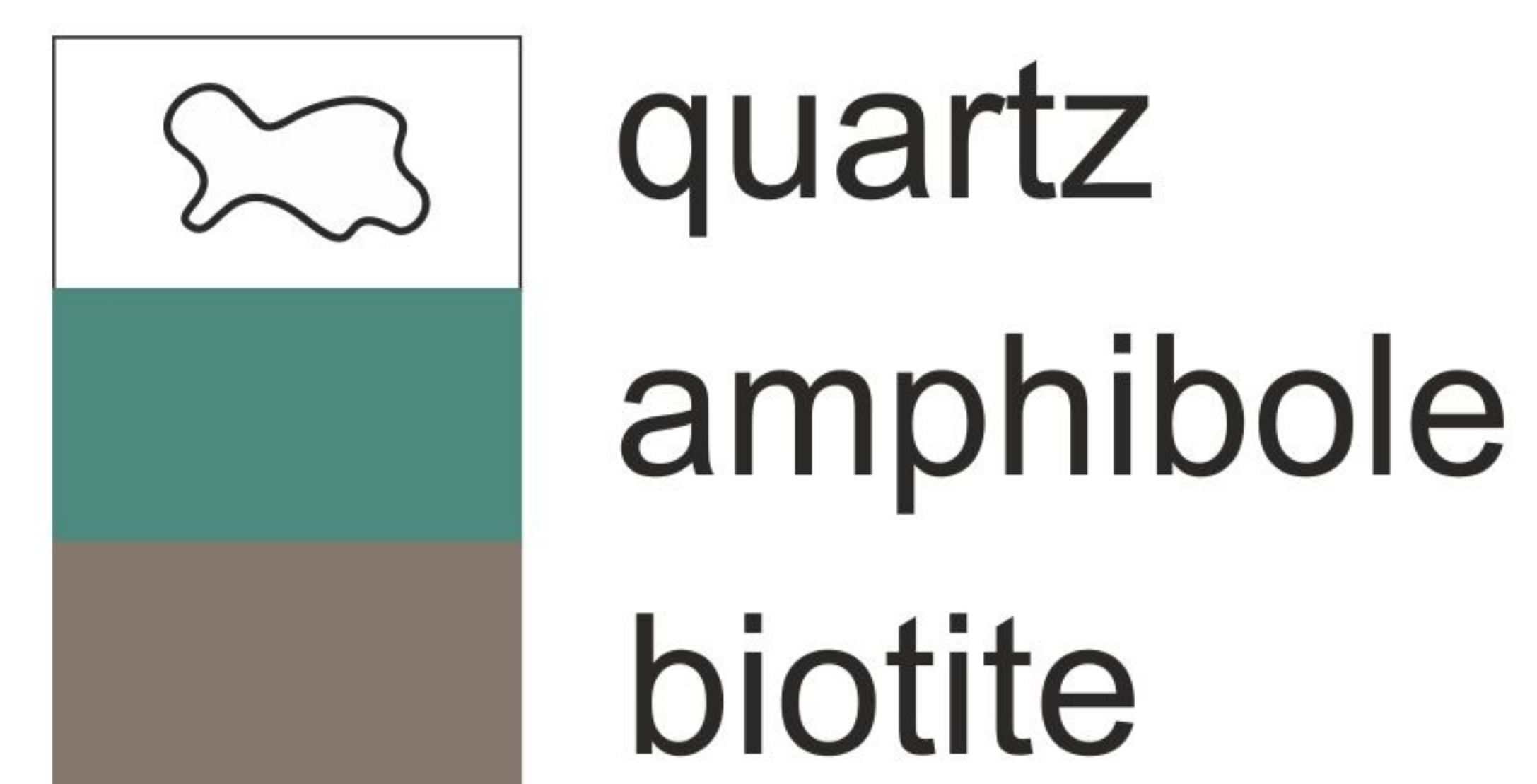


Figure 7.

$$\dot{\epsilon}_{\text{AMBIORL}} = (2.34 \text{ to } 3.43) \times \dot{\epsilon}_{\text{CGQL}}$$

MICRO SCALE
(mylonitized amphibolite)

CGQL

$$w = 152.3 \mu\text{m}$$

$$d = 0.92 \text{ cm}$$

AMBIORL

$$w' = 197.1 \mu\text{m}$$

$$d' = 2.79\text{-}4.1 \text{ cm}$$

a

$$\dot{\epsilon}_{\text{layer 2}} = (2.34 \text{ to } 3.43) \times \dot{\epsilon}_{\text{layer 1}}$$

OUTCROP SCALE
(hypothetical)

hypothetical
layer 1

$$w = 10 \text{ m}$$

$$d = 605 \text{ m}$$

hypothetical
layer 2

$$w' = 10 \text{ m}$$

$$d' = 1416\text{-}2075 \text{ m}$$

b

$$\dot{\epsilon}_{\text{layer 2}} = (2.34 \text{ to } 3.43) \times \dot{\epsilon}_{\text{layer 1}}$$

REGIONAL SCALE
(hypothetical)

hypothetical
layer 1

$$w = 1.25 \text{ km}$$

$$d = 75.625 \text{ km}$$

hypothetical
layer 2

$$w' = 1.25 \text{ km}$$

$$d' = 177 \text{ to } 259.37 \text{ km}$$

c

2.5 km